

Two-dimensional crystal melting and D4-D2-D0 on toric Calabi-Yau singularities

Takahiro Nishinaka^{1 a}, Satoshi Yamaguchi^{2 b} and Yutaka Yoshida^{3 c}

^a*NHETC and Department of Physics and Astronomy, Rutgers University,
126 Frelinghuysen Rd., Piscataway, NJ 08855, USA*

^b*Department of Physics, Graduate School of Science, Osaka University,
Toyonaka, Osaka 560-0043, Japan*

^c*High Energy Accelerator Research Organization (KEK),
Tsukuba, Ibaraki 305-0801, Japan*

Abstract

We construct a two-dimensional crystal melting model which reproduces the BPS index of D2-D0 states bound to a non-compact D4-brane on an arbitrary toric Calabi-Yau singularity. The crystalline structure depends on the toric divisor wrapped by the D4-brane. The molten crystals are in one-to-one correspondence with the torus fixed points of the moduli space of the quiver gauge theory on D-branes. The F- and D-term constraints of the gauge theory are regarded as a generalization of the ADHM constraints on instantons. We also show in several examples that our model is consistent with the wall-crossing formula for the BPS index.

¹nishinaka [at] physics.rutgers.edu

²yamaguch [at] het.phys.sci.osaka-u.ac.jp

³yyoshida [at] post.kek.jp

Contents

1	Introduction and summary	2
2	Crystal melting for D6-D2-D0 states	6
2.1	Quivers on D2-D0 from brane tilings	7
2.2	Adding a flavor D6-node	11
2.3	Moduli space and θ -stable modules	11
2.4	BPS index and molten crystals	13
3	Crystal melting for D4-D2-D0 states	16
3.1	Isoradial embedding	17
3.2	Flavor D4-node	18
3.3	Moduli space of vacua	20
3.4	Two-dimensional melting crystal	24
3.5	Shape of the crystal	25
3.6	Partition function	28
3.7	Proof of $J = 0$	29
3.8	Proof of $m_{\mathcal{D}} = 0$	38
4	Examples	40
4.1	\mathbb{C}^3	40
4.2	Conifold	43
4.3	Suspended pinch point	46
4.4	Orbifold $\mathbb{C}^2/\mathbb{Z}_N \times \mathbb{C}$	57
A	Stability condition	65
B	Isoradial dimer model	65
C	Perfect matching and toric divisor	66

1 Introduction and summary

The geometry near D-branes is probed by lighter branes bound to them. One of the most well-known examples is that Dp -branes bound to $D(p+4)$ -branes on the orbifold $\mathbb{C}^2/\mathbb{Z}_N$ describe instantons on the resolved A_{N-1} ALE space [1].

Recently, there has been remarkable progress in the study of D0-D2 states bound to a D6-brane on a toric Calabi-Yau three-fold. From the above viewpoint, such D-branes probe the Calabi-Yau geometry wrapped by the D6-brane. In fact, the BPS index of the D-brane bound states is evaluated by counting the molten configurations of a three-dimensional crystal [2, 3, 4, 5, 6], whose crystalline structure is determined by the toric diagram of the background Calabi-Yau three-fold [5].⁴ Moreover, the thermodynamic limit of the molten crystal describes the smooth geometry of the mirror Calabi-Yau three-fold [11, 12]. This suggests that the melting crystal gives a “discretization” of the background Calabi-Yau geometry.

The generalization of the crystal melting model to D4-D2-D0 states has partially been studied. In [13, 14], the authors considered D2-D0 states bound to a non-compact D4-brane on a divisor of the (generalized) conifold, and constructed a *two-dimensional* statistical model which reproduces the BPS index of the D4-D2-D0 states. After the success of the D6-D2-D0 crystal melting, it is natural to expect that the structure of the two-dimensional model is related to some property of the toric divisor wrapped by the D4-brane. However, such a relation has not yet been clarified. The main reason for this is that the prescription given in [13, 14] is *ad hoc* and not derived from the BPS condition for the D-brane bound states.

In this paper, we derive a general method to construct a *two-dimensional* crystal melting model for D4-D2-D0 states on an arbitrary toric Calabi-Yau three-fold, by solving the BPS condition for the D-branes. We put a D4-brane on a non-compact toric divisor \mathcal{D} of a toric Calabi-Yau three-fold Y , and count BPS D2-D0 states bound to it. Here the D2-branes are wrapped on compact two-cycles of Y , and the D0-branes are point-like in Y . We particularly consider the singular limit of Y , in which D2-D0 states are realized as fractional branes localizing at the singularity. We identify the supersymmetric gauge theory on the D-branes, and solve the F- and D-term constraints. There is a natural torus action on the moduli space \mathcal{M}_{D4} of supersymmetric vacua, which essentially comes from the toric action on Y . We then show that the torus fixed points of \mathcal{M}_{D4} are in one-to-one correspondence with the molten configurations of a *two-dimensional* crystal. The crystalline structure depends on the choice of the divisor wrapped by the D4-brane.

To give a short summary of this paper, let us first consider the simplest case of $Y = \mathbb{C}^3$ and $\mathcal{D} = \mathbb{C}^2 \subset Y$. Since \mathbb{C}^3 has no compact two-cycle, we can only consider

⁴There are also several works on the crystal melting description of the wall-crossing phenomena [7, 8, 9] and refinement [10].

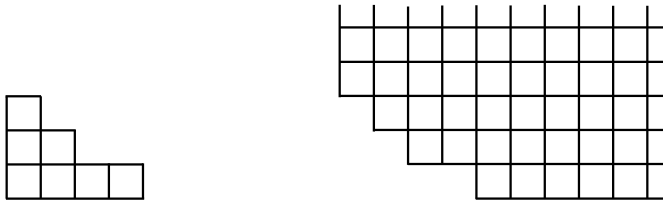


Figure 1: A Young diagram (left) can be regarded as a molten configuration of a two-dimensional crystal (right). The crystal infinitely extends in the upper-right region.

D4-D0 states. The low-energy effective theory on k D0-branes bound to a D4-brane on \mathcal{D} is a $d = 1$ supersymmetric $U(k)$ gauge theory with 8 supercharges. In the $d = 4, \mathcal{N} = 2$ language, the theory includes three adjoint chiral multiplets B_a for $a = 1, 2, 3$ which come from D0-D0 strings with the usual $\mathcal{N} = 4$ superpotential

$$\text{tr}(B_1[B_2, B_3]). \quad (1.1)$$

There are also a fundamental and an anti-fundamental chiral multiplet I, J which come from D4-D0 strings with the $\mathcal{N} = 2$ superpotential⁵

$$JB_3I. \quad (1.2)$$

The well-known fact is that the F-term conditions for the above superpotential imply the ADHM constraints on k -instantons:⁶

$$[B_1, B_2] + IJ = 0. \quad (1.3)$$

Here, the effect of the non-compact D4-brane clearly appears in the additional superpotential (1.2). The moduli space \mathcal{M}_{D4} of supersymmetric vacua admits a natural torus action. The BPS index is essentially equivalent to the number of the torus fixed points of \mathcal{M}_{D4} , which are labeled by Young diagrams [15, 16]. Note that each Young diagram is regarded as a molten configuration of a two-dimensional crystal composed of square boxes (figure 1). Therefore, counting the torus fixed points is equivalent to counting the molten crystals. The aim of this paper is to generalize this to arbitrary Y and \mathcal{D} .

When Y is a general toric Calabi-Yau three-fold and \mathcal{D} is one of its toric divisors, the low-energy effective theory on D-branes is identified by using the technique of

⁵Here we assume without loss of generality that B_3 describes the fluctuations of the D0-branes in directions transverse to the D4-brane.

⁶The real part of the ADHM constraints comes from the D-term constraint.

brane tiling [5]. In section 2, we briefly review the work [5] on the crystal melting model for D6-D2-D0 states on a toric Calabi-Yau three-fold, including the technique of brane tiling. The brane tiling was originally developed in the study of the D-brane construction of $\mathcal{N} = 1$ supersymmetric gauge theories [17, 18, 19, 20] (For reviews, see also [21, 22]). We particularly study brane tilings with so-called isoradial embedding, as mentioned in subsection 3.1. The main difference from the D6-D2-D0 case is that the D4-brane induces an additional superpotential such as (1.2). In subsection 3.2, we use a technique developed in [23] to identify such an additional potential for arbitrary Y and \mathcal{D} . We then claim in subsection 3.3 that the F- and D-term constraints imply that some chiral multiplets have vanishing vev's on supersymmetric vacua. In the above example of $Y = \mathbb{C}^3$, B_3 is such a chiral multiplet. The set of chiral multiplets with vanishing vev's is specified by a so-called “perfect matching.” The proof of our claim is given in subsections 3.7 and 3.8, where we use the results of [24]. Based on this observation, we show that the resulting moduli space \mathcal{M}_{D4} is embedded in the moduli space \mathcal{M}_{D6} of the parent D6-D2-D0 state. Here, the parent D6-D2-D0 state is obtained by replacing the D4-brane with a D6-brane wrapping on the whole Calabi-Yau Y . The inclusion map $i : \mathcal{M}_{D4} \hookrightarrow \mathcal{M}_{D6}$ is characterized by the perfect matching. We then show in subsection 3.4 that the torus fixed points of \mathcal{M}_{D4} are in one-to-one correspondence with the molten configurations of a two-dimensional crystal. *This two-dimensional crystal is, in fact, a “slope face” of the three-dimensional crystal associated with the parent D6-D2-D0 counting.* Moreover, choosing a different divisor \mathcal{D} of the same Calabi-Yau Y gives a *different* slope face of the *same* three-dimensional crystal. As described in 3.5, the boundary of the two-dimensional crystal is given by so-called “zig-zag paths.”

In section 4, we give several examples in which Y is \mathbb{C}^3 , the conifold, the suspended pinch point, and the orbifold $\mathbb{C}^2/\mathbb{Z}_N \times \mathbb{C}$. In particular, when Y is the conifold, our crystal melting model reproduces the triangular partition model proposed in [13]. If Y is the suspended pinch point, our model reproduces the oblique partition model proposed in [14]. Furthermore, when $Y = \mathbb{C}^2/\mathbb{Z}_N \times \mathbb{C}$ and $\mathcal{D} = \mathbb{C}^2/\mathbb{Z}_N \subset Y$, our model reproduces the orbifold partition model [25, 26, 27] whose partition function agrees with the $\mathcal{N} = 4$ $U(1)$ instanton partition function on the A_{N-1} ALE space, i.e. the level-one character of the affine $SU(N)$ algebra. Note that this example is the original setup of [1], which has been mentioned at the very beginning. In fact, our setup is a generalization of that of [1] to an arbitrary toric divisor. In some of the examples, we explicitly show that our model is consistent with the wall-crossing

formula for the BPS index.

One of interesting future works is to extend our result to the multiple D4-branes with D2- and D0-branes. When $Y = \mathbb{C}^2/\mathbb{Z}_N \times \mathbb{C}$ and $\mathcal{D} = \mathbb{C}^2/\mathbb{Z}_N \subset Y$, this setup produces the affine Lie algebra character with a higher level than one. It will also be an interesting future problem to assign certain weights to each fixed point of $U(1)^2$ in the moduli space and study an analogue of the Nekrasov's partition function [16, 28]. This generalization should have a good realization in the string theory and the M-theory. Furthermore it should be related to some observables of a 2-dimensional conformal field theory by the AGT relation [29]. From the viewpoint of the gauge theory on the D4-brane, this work can be thought of as the instanton counting in the $d = 4, \mathcal{N} = 4$ supersymmetric gauge theory on a toric divisor.⁷ There are several interesting works [31, 32, 33] on the crystal melting in this context. It is worth studying the relation to these works. It would also be interesting to apply our method to a Calabi-Yau three-fold with compact four-cycles. Although we do not explicitly consider such an example in this paper, the application is straightforward. When Y contains compact four-cycles, the melting crystals also count the charge for compact D4-branes. In particular, it would be interesting to study the relation to the work of [34]. Another interesting direction would be to study the connection to the works [35, 36, 37, 38, 39], where the crystal melting model was studied in the context of five-dimensional supersymmetric gauge theories. It is also worth studying the relation to the works [40, 41, 42, 43] on the BPS chiral operators of gauge theories on D-branes at toric Calabi-Yau singularities.

2 Crystal melting for D6-D2-D0 states

We here briefly review the crystal melting model for D6-D2-D0 states on a toric Calabi-Yau singularity, mainly following [5]. We consider the BPS bound states of a single non-compact D6-brane and arbitrary numbers of D2 and D0 branes, where the D6-brane is wrapping the whole Calabi-Yau, the D2-branes are wrapping compact two-cycles and the D0-branes are point-like in the Calabi-Yau three-fold.

⁷To be more precise, the theory is a topologically twisted $\mathcal{N} = 4$ super Yang-Mills theory. The fact that the divisor is embedded in a Calabi-Yau three-fold implies that the topological twist is the Vafa-Witten type twist [30].

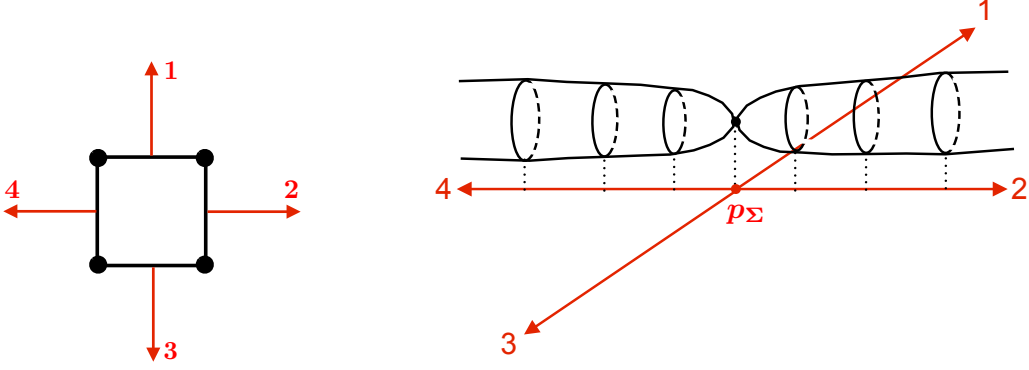


Figure 2: Left: The toric diagram of the conifold. Each line segment s corresponds to a non-compact curve β_s in the conifold. Right: The corresponding T^2 -fiber. We have a non-degenerate T^2 -fiber at a generic point of the toric base \mathbb{R}^3 . However, the T^2 degenerates to S^1 along some semi-infinite lines from p_Σ . The semi-infinite lines are in one-to-one correspondence with the curves β_s . At the intersection p_Σ , the T^2 -fiber shrinks into a point, giving rise to a singularity.

2.1 Quivers on D2-D0 from brane tilings

A toric Calabi-Yau three-fold Y_Σ is roughly regarded as a $(T^2 \times \mathbb{R})$ -bundle over \mathbb{R}^3 , where the T^2 -fiber degenerates in a subspace specified by a toric diagram Σ . We mainly consider Y_Σ without compact 4-cycles. The toric diagram Σ is a convex lattice polygon, in which every vertex is associated with a toric divisor of Y_Σ . Every line segment s in Σ is associated with a non-compact curve β_s in Y_Σ , along which the T^2 -fiber degenerates to S^1 . The degenerate cycle is specified by the slope of the line segment s . Namely, if s is stretched between two vertices (p_1, q_1) and (p_2, q_2) in Σ , then $(q_1 - q_2, -p_1 + p_2)$ -cycle of T^2 degenerates along the curve β_s . The transverse $(p_1 - p_2, q_1 - q_2)$ -cycle then generates an isometry of the curve β_s . At the intersection p_Σ of all the curves β_s , the T^2 -fiber shrinks into a point, giving rise to a singularity (See figure 2).

Let us consider D0-branes localized at the singularity p_Σ . In order to evaluate the supersymmetric index for such BPS D0-branes, we identify the low energy effective theory on the D0-branes. We first take the T-duality transformation along the two directions of the T^2 -fiber, which maps the D0-branes to D2-branes wrapping on the whole T^2 . On the other hand, the toric Calabi-Yau geometry itself is mapped to intersecting NS5-branes in flat spacetime [44, 45, 18, 46] because the T-duality exchanges

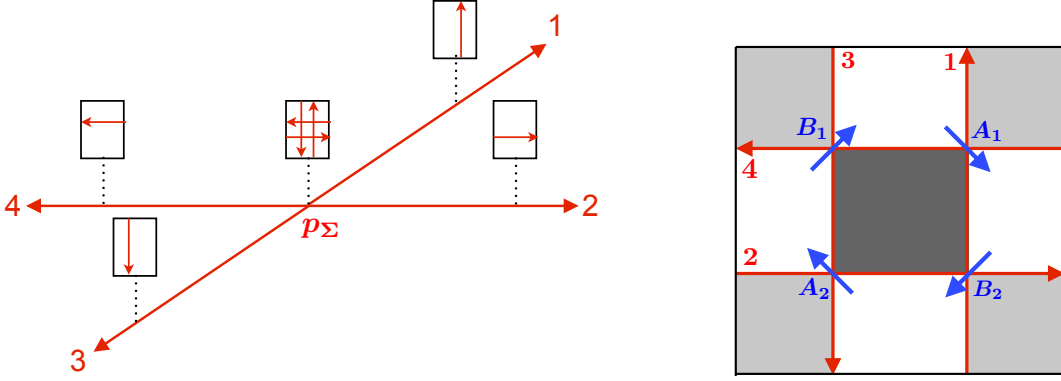


Figure 3: Left: Each NS5-brane is a semi-infinite line in the toric base and wrapped on a one-cycle of the T^2 -fiber. Right: All the NS5-branes intersect at the point p_Σ , where we have a brane tiling system. The red lines are the NS5-branes, which “bend” to fill up the gray regions. In the white regions, we only have dynamical D-branes without NS5-branes. Each blue arrow is associated with a massless chiral multiplet.

the source of the KK gauge field with that of the NSNS B-field. To be more concrete, the curve β_s for every line segment s of Σ is mapped to a single NS5-brane wrapped on a semi-infinite tube. The tube is an S^1 -fibration over a semi-infinite line from p_Σ in the toric base. If s is stretched between (p_1, q_1) and (p_2, q_2) , then the S^1 is the $(p_1 - p_2, q_1 - q_2)$ -cycle of the T^2 -fiber (See figure 3). The NS5-branes also extend in \mathbb{R}^4 transverse to the six-dimensional space we are considering.

The D2-branes wrapping on T^2 , which come from the original D0-branes, are now divided into several “tiles” by the intersecting NS5-branes (figure 3). Here, the conservation of the NS5-charge implies [47] that the intersecting NS5-branes in fact “bend” to fill up some of the tiles (The gray regions in figure 3). To be more precise, if the boundary NS5-branes of a tile gives a definite orientation, the tile is filled with an NS5-brane. Such tiles are classified into two types, depending on the orientations of the NS5-brane. In figure 3, the dark and light gray regions are filled with NS5-branes with opposite orientations. The white regions has no NS5-branes, and are filled only with the D-branes. By construction, neither two gray regions nor two white regions share any edge. Furthermore, the corner of a light gray region is attached to the corner of a dark gray region, and vice versa.

Now, we consider the low-energy effective theory on the D-branes. When we reduce the two directions of T^2 , we obtain a supersymmetric quantum mechanics on the

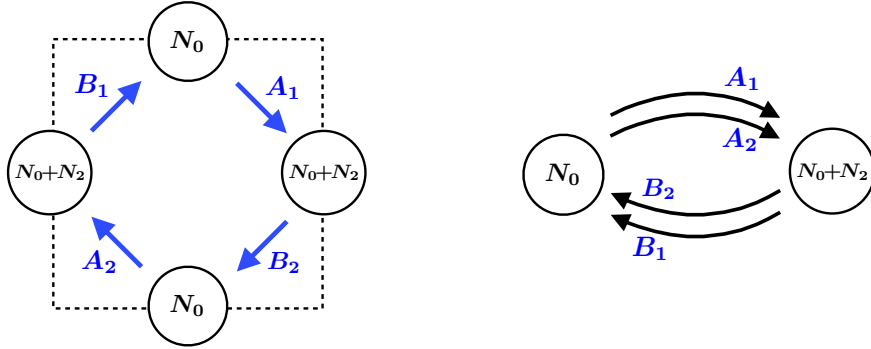


Figure 4: Left: The quiver diagram Q associated with the brane tiling in figure 3. The diagram is defined on T^2 ; The upper (right) and lower (left) dotted lines are identified. Here N_0 and N_2 are the D0- and D2-charges on the conifold, respectively. Right: The left quiver diagram is equivalent to the well-known quiver for the conifold.

world-volume of the D-branes, whose field content can be read off from the brane configuration in T^2 . Each white region in T^2 gives a $U(N_0)$ gauge group, where N_0 is the original D0-brane charge. The gray regions give rise to no gauge multiplet because they are filled with NS5-branes. We also have a bifundamental (or adjoint) multiplet at each intersection point of the white regions. Such a bifundamental is expressed as an arrow from one white region to the other (figure 3). The orientation of the arrow is determined by the relative positions of two adjacent gray regions. We determine it so that the arrow goes from bottom to top when the adjacent *light* gray region is on its *left* side.⁸ This definite orientation means that the bifundamental (or adjoint) is not a hyper multiplet but a chiral multiplet. Thus, the low-energy theory on the D-branes is a $d = 1, \mathcal{N} = 4$ quiver quantum mechanics. For example, the quiver diagram for the brane configuration in figure 3 is shown in figure 4. For a given quiver diagram Q on T^2 , we denote by Q_0 the set of nodes in Q , as well as by Q_1 the set of arrows in Q . The set of faces in Q is denoted by Q_2 . We sometimes denote by \tilde{Q} the universal cover of the quiver diagram Q .

The superpotential for the chiral multiplets comes from string disk amplitudes associated with the gray regions. If a light gray region is surrounded by the chain of arrows X_1, \dots, X_n , then there is a superpotential term of the form

$$\text{tr}(X_1 \cdots X_n). \quad (2.1)$$

⁸Of course, the adjacent *dark* gray region is on the *right* side of the arrow.

Here we used the same symbol X_a to denote a chiral multiplet associated with the arrow X_a . On the other hand, a dark gray region contributes

$$- \operatorname{tr} (X_1 \cdots X_m) \tag{2.2}$$

to the superpotential if it is surrounded by the chain of the arrows X_1, \dots, X_m . The minus sign here is due to the opposite orientation of the NS5-branes. Since each arrow is attached to one light gray and one dark gray region, every chiral multiplet appears twice in the superpotential.⁹

So far we have only considered D0-branes at the original Calabi-Yau three-fold Y_Σ , which leads to the same rank of the gauge groups. Now, let us consider additional D2-branes wrapping on some compact two-cycles of Y_Σ . In the singular Calabi-Yau limit, all the compact cycles are vanishing and the D2-charge is realized as the fractional D0-charge. For example, when we originally have N_2 D2-branes on a vanishing two-cycle, the T-duality maps them to D2-branes which fills one of the white regions in T^2 , increasing the rank of the corresponding gauge group by N_2 (figure 4). Thus, introducing D2-charges changes the rank of the gauge groups.

We have seen that the T-duality maps the toric Calabi-Yau geometry to the brane tiling system, from which we can read off the quiver diagram Q on T^2 and the superpotential. Let us here mention the dual diagram Q^\vee of Q . Namely, we consider a graph Q^\vee on T^2 such that $Q_0^\vee \simeq Q_2$, $Q_1^\vee \simeq Q_1$ and $Q_2^\vee \simeq Q_0$. In Q^\vee , every face is associated with a gauge group while every vertex gives a superpotential term. Every line segment is associated with a chiral multiplet. We denote this dual map by $\psi : Q \rightarrow Q^\vee$. We sometimes denote the universal cover of Q^\vee by \tilde{Q}^\vee . We assign the color of white or black to a vertex $f \in Q_0^\vee$, depending on the orientation of the corresponding face $\psi^{-1}(f)$. If $\psi^{-1}(f)$ is a light gray (dark gray) face, then we assign white (black) to f . Then, it follows from our construction that the dual diagram Q^\vee is a *bipartite graph* where any line segment connects one black and one white vertex (figure 5). In mathematics, such Q^\vee defines a *dimer model* on T^2 . Therefore, we sometimes call vertices in Q_0^\vee “dimer vertices” while those in Q_0 “quiver vertices.” This dimer model Q^\vee plays an important role in the main part of this paper.

⁹This implies that we can set all the coupling constant in W to be +1 or -1 by rescaling the superfield X_i . In (2.1) and (2.2), we have already taken into account such rescalings.

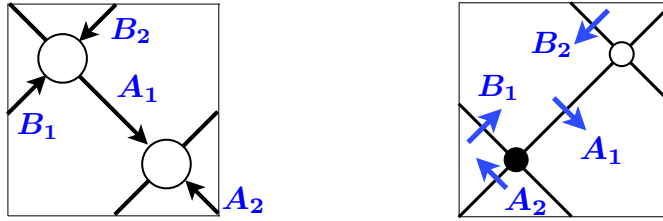


Figure 5: The quiver diagram Q (left) and the dual graph Q^\vee (right) on T^2 . Each vertex in Q^\vee is black or white colored, depending on the orientation of the dual face in Q . By construction, Q^\vee is always a bipartite graph, giving a dimer model on T^2 .

2.2 Adding a flavor D6-node

We now put an additional D6-brane wrapping on the whole Calabi-Yau Y_Σ . Since such a D6-brane is non-compact, we can regard it as a flavor brane. In the quiver language, it adds an additional flavor node $*$ to the quiver diagram Q . Note that the T-duality maps the D6-brane to a non-compact D4-brane localized at a point in T^2 . We assume that the point is attached to a white tile in the brane tiling. Then the quiver has an arrow I from $*$ to an another node $i \in Q_0$, which describes a “quark” in the fundamental representation of the gauge group associated with i . Thus, adding a single D6-brane implies an extended quiver \widehat{Q} with $\widehat{Q}_0 = Q_0 \cup \{*\}$ and $\widehat{Q}_1 = Q_1 \cup \{I\}$. Since there is no gauge invariant operators involving I , we have no additional superpotential induced by the D6-brane. From the mathematical viewpoint, the flavor node $*$ gives a “framing” for quiver representations.

2.3 Moduli space and θ -stable modules

The D-brane bound states we are considering can be seen as BPS particles in \mathbb{R}^4 , and our aim is to evaluate the BPS index of such BPS particles. Since the D-brane world-volume itself breaks half the supersymmetry, the BPS index is regarded as the Witten index of the quiver quantum mechanics on the D-branes. To evaluate the Witten index, we first have to identify the moduli space of supersymmetric vacua.

The moduli space of the world-volume theory is parameterized by the supersymmetric configurations of scalar fields. Some of the scalars correspond to fluctuations of the D-branes in the Calabi-Yau three-fold Y_Σ , while the others express fluctuations in \mathbb{R}^3 . Here the latter describes the position of the BPS particle in \mathbb{R}^3 and we fix it. Then the remaining moduli space is exactly the same as the moduli space of a $d = 4, \mathcal{N} = 1$

quiver gauge theory with the same quiver diagram \widehat{Q} and the superpotential W . Below, we describe this moduli space in terms of quiver representations.

We first define the so-called “path-algebra” $\mathbb{C}\widehat{Q}$ which is generated by paths in the quiver diagram \widehat{Q} . Any path in \widehat{Q} starts at a node, follows some arrows and terminates at a node. The product of two paths is defined by connecting the tail of the first path with the head of the second path. Here, if the tail of the first and the head of the second are not attached to the same quiver node, the product is defined to be zero. For each node $\ell \in \widehat{Q}_0$, there is a special element e_ℓ of $\mathbb{C}\widehat{Q}$ which corresponds to a path from ℓ to ℓ with zero length. Since e_ℓ is regarded as the projection onto the set of paths terminating at ℓ , the element $\sum_{\ell \in \widehat{Q}_0} e_\ell$ is the multiplicative identity of the path algebra $\mathbb{C}\widehat{Q}$. Physically, a $\mathbb{C}\widehat{Q}$ -module corresponds to a configuration of chiral fields in the quiver quantum mechanics, which might break supersymmetry.

In order to impose the F-flat condition, we consider a quotient

$$A = \mathbb{C}\widehat{Q}/\mathcal{F} \tag{2.3}$$

where \mathcal{F} is the ideal of $\mathbb{C}\widehat{Q}$ generated by all the derivatives $\partial W/\partial X_a$ for $X_a \in Q_1$.¹⁰ Physically, an A -module expresses a F-flat configuration of the chiral fields. Note here that an A -module M has a natural grading $M = \bigoplus_{\ell \in \widehat{Q}_0} M_\ell$ where $M_\ell = e_\ell M$. Since A includes a subalgebra isomorphic to \mathbb{C} , each module M_k is naturally a complex vector space. For each $k \in Q_0$, $\dim M_k$ is identified with the rank of the gauge group associated with the node k . On the other hand, $\dim M_*$ expresses the rank of the flavor symmetry group associated with the D6-node. Since we only have a single D6-brane, we set $\dim M_* = 1$.

On the other hand, the D-flatness condition is known to be equivalent to the θ -stability [48] defined as follows. For a given set of real parameters θ_k for all $k \in Q_0$ and θ_* , the slope function of an A -module M is defined by

$$\theta(M) = \sum_{k \in Q_0} \theta_k \dim M_k + \theta_* \dim M_*. \tag{2.4}$$

Now, for a given A -module M , we fix θ_k, θ_* so that $\theta(M) = 0$. Then, M is called θ -stable if every non-zero proper sub-module $M' \subset M$ satisfies $\theta(M') < 0$.¹¹ In [48], it was shown that θ -stable modules with complexified gauge groups are in one-to-one

¹⁰Here we denote a path corresponding to an arrow X_i by the same symbol X_i .

¹¹We here use the opposite inequality sign in comparison to [48], which is just a matter of convention.

correspondence with the D-flat configurations, where θ_k, θ_* are identified with the FI parameters of the quiver gauge theory. The condition $\theta(M) = 0$ is easily understood when identifying θ_k, θ_* with the FI parameters. In fact, the D-term conditions are schematically written as

$$\sum_{X_a \in S_\ell} X_a^\dagger X_a - \sum_{X_a \in T_\ell} X_a X_a^\dagger = \theta_\ell \mathbf{1}, \quad (2.5)$$

where S_ℓ and T_ℓ are the sets of arrows in \widehat{Q}_1 which start and end at $\ell \in \widehat{Q}_0$ respectively. Summing up the trace of (2.5) for all $\ell \in \widehat{Q}_0$, we obtain $\theta(M) = 0$. This implies that there are $|Q_0|$ independent θ -parameters for a given A -module. In this paper, we always set θ so that $\theta_k < 0$ for all $k \in Q_0$. Note that this implies $\theta_* \geq 0$. Changing the θ -parameters generically gives rise to the wall-crossing phenomena of the BPS states. For more on the stability condition, see appendix A.

From this argument, we can see that θ -stable A -modules are in one-to-one correspondence with the supersymmetric vacua of the quiver quantum mechanics. In the next subsection, we use this correspondence to study the torus fixed points of the moduli space. In particular, we use the fact that *any θ -stable A -module M with $\theta_k < 0$ for all $k \in Q_0$ is a cyclic module generated by an element $\mathfrak{m} \in M_*$, that is, $M = A\mathfrak{m}$ [7]. In fact, if $A\mathfrak{m} \neq M$ then $A\mathfrak{m}$ is a proper submodule of M with $\theta(A\mathfrak{m}) > 0$, which contradicts with the θ -stability of M . Note that, since M_* is one-dimensional, such an element \mathfrak{m} is essentially unique.*

2.4 BPS index and molten crystals

We now come to the main part of this section. We evaluate the Witten index in terms of the θ -stable A -modules. First of all, the Witten index can be calculated via the localization with respect to $U(1)^3 = U(1)^2 \times U(1)_R$ action on the moduli space. Here, $U(1)^2$ comes from the toric actions on the Calabi-Yau three-fold Y_Σ while $U(1)_R$ is the R-symmetry of the theory.¹²

To see the $U(1)^3$ -actions explicitly, let us consider a map $t : Q_1 \rightarrow U(1)$. Such a map assigns a global $U(1)$ -action to each chiral multiplet. We require that t keeps all the F-term conditions, or equivalently, t keeps the superpotential up to an overall rescaling. We denote the set of all such t by T . Since the D-term constraints are obviously invariant under $t \in T$, the moduli space of supersymmetric vacua is symmetric under

¹²To be more precise, $U(1)_R$ is the R-symmetry of the parent $d = 4, \mathcal{N} = 1$ supersymmetry of our $d = 1, \mathcal{N} = 4$ quiver quantum mechanics.

the action of T . Let us consider how many independent t -actions there are. For each face $f \in Q_2$, we define

$$n_f = \prod_{X \in \partial f} t(X), \quad (2.6)$$

where the product is taken over chiral fields surrounding f . Preserving the F-term conditions is equivalent to requiring that the ratio n_{f_1}/n_{f_2} is precisely invariant for any $f_1, f_2 \in Q_2$. Note that the ratios are not all independent because there is an identity

$$\prod_{f \in Q_2} n_f^{\text{sign}(f)} = 1, \quad (2.7)$$

where $\text{sign}(f) = \pm 1$ depending on the color (light or dark gray) associated with the face f . This identity follows from the fact that any chiral field is attached to one dark and one light gray region. Due to this, there are only $(|Q_2| - 2)$ independent ratios n_{f_1}/n_{f_2} . Requiring all of them invariant imposes $(|Q_2| - 2)$ constraints on the t -actions.¹³ We then find $T \simeq U(1)^{|Q_1| - (|Q_2| - 2)}$.

Note that some of the t -actions are absorbed into gauge transformations. In the $U(1)^{|Q_0|}$ subgroup of the gauge group, the diagonal $U(1)$ keeps all the chiral fields invariant. The other $U(1)^{|Q_0| - 1}$ can absorb $(|Q_0| - 1)$ degrees of freedom of T . The independent global symmetry of the theory is thus $T/U(1)^{|Q_0| - 1} \simeq U(1)^3$, where we used the Euler formula for T^2 : $|Q_0| - |Q_1| + |Q_2| = 0$. This means that each t -action is an $U(1)^3$ -action modulo gauge transformations. Since θ -stable A -modules are generated by a single element \mathfrak{m} , this $U(1)^3$ -action is naturally extended to the modules, where we set \mathfrak{m} to be invariant under T .

The $U(1)^3$ -fixed points of the moduli space are equivalent to $U(1)^3$ -invariant θ -stable A -modules. It was shown in [4] that the latter is in one-to-one correspondence with so-called “finite ideals” defined as follows. We first define Δ_* to be the set of the F-term equivalence classes of paths starting at the node $*$. For any $[x], [y] \in \Delta_*$, we write $[x] \leq [y]$ if there is a path z and representatives x, y of $[x], [y]$ so that $y = zx$. Then, a finite ideal π of Δ_* is defined as a subset of Δ_* with the following property:

$$\text{For any } [x], [y] \in \Delta_* \text{ satisfying } [x] \leq [y], \text{ if } [y] \in \pi \text{ then } [x] \in \pi.$$

For a given finite ideal π of Δ_* , an A -module spanned by all the elements in π is a $U(1)^3$ -invariant θ -stable module. On the other hand, any $U(1)^3$ -invariant θ -stable module

¹³As we will see later, there are equal numbers of faces with $\text{sign}(f) = +1$ and those with $\text{sign}(f) = -1$. This guarantees that the identity (2.7) is consistent with the overall rescaling of the superpotential.

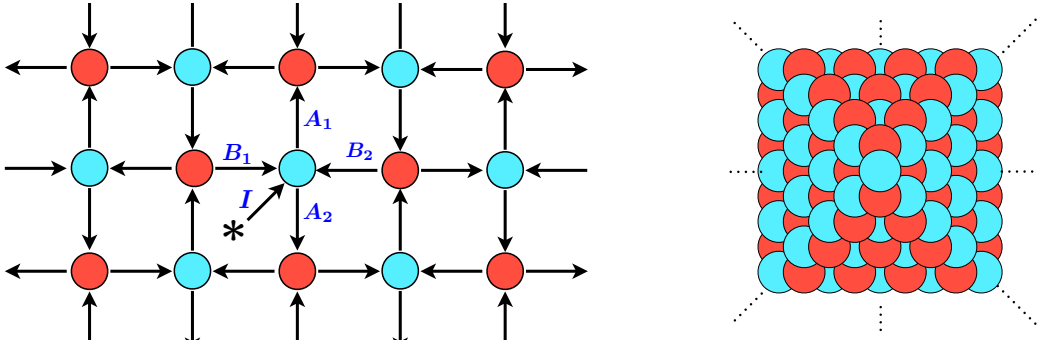


Figure 6: Left: The periodic quiver \tilde{Q} for the conifold case, which is the universal cover of the quiver diagram Q on T^2 . Right: The three-dimensional crystal C_{Δ_*} is obtained by putting atoms for all the elements of Δ_* . Each finite ideal of Δ_* corresponds to a molten configuration of the crystal.

has its basis corresponding to a finite ideal of Δ_* . This is clearly a generalization of the fact that the torus fixed points of the moduli space of instantons in \mathbb{C}^2 are labeled by Young diagrams.

What is important here is that the finite ideals of Δ_* are expressed as molten crystals [5]. To see this, we first consider the universal cover \tilde{Q} of the quiver diagram Q , which is also attached to a D6-node $*$ at a reference node (figure 6). We call \tilde{Q} the periodic quiver. We now start at $*$ and follow all the F-term equivalence classes of paths in Δ_* , putting an “atom” on the ending node of each path. From the dimer model viewpoint, we place an atom on a face of \tilde{Q}^\vee . An atom on $k \in \tilde{Q}_0$ has its “color” determined by $p(k)$ where $p : \tilde{Q} \rightarrow Q$ is the natural projection. When we consider two different equivalence classes $[c_1], [c_2] \in \Delta_*$ ending at the same node $k \in \tilde{Q}_0$, we need to consider the “depth” of atoms. It was shown in [4] that any path from $*$ to a node $k \in \tilde{Q}_0$ is F-term equivalent to $v_k \omega^\ell$ for some $\ell \in \mathbb{N}$, where v_k is the shortest path from $*$ to k and ω is a loop around some face of \tilde{Q} .¹⁴ Here ω and v_k are not unique, but the integer ℓ is uniquely determined. Thus, the elements of Δ_* are completely classified by its ending node $k \in \tilde{Q}_0$ and the integer ℓ . Then, we determine that for a F-term equivalence class $[v_k \omega^\ell] \in \Delta_*$ we put an atom on the node k at the depth ℓ . If we put atoms for all the elements of Δ_* , we obtain a three-dimensional crystal C_{Δ_*} on the periodic quiver \tilde{Q} (figure 6). Note here that there is a bijection $f : \Delta_* \rightarrow C_{\Delta_*}$. For

¹⁴To be precise, this equivalence relies on some conditions on the dimer model. In this paper, we only consider dimer models with “isoradial embedding” as explained in subsection 3.1. For such dimer models, all the conditions are satisfied [4, 24, 49, 50].

any two atoms $\alpha, \beta \in C_{\Delta_*}$, we say that there is a “bond” from α to β if there is an arrow from $f^{-1}(\alpha)$ to $f^{-1}(\beta)$. It is now clear that a finite ideal of Δ_* corresponds to a subcrystal \mathfrak{p} of C_{Δ_*} such that

$$\text{a bond from } \beta \in C_{\Delta_*} \text{ to } \alpha \in \mathfrak{p} \text{ implies } \beta \in \mathfrak{p}.$$

Now, recall that the Witten index of the quiver quantum mechanics on D-branes is evaluated as a sum over the $U(1)^3$ -fixed points of the moduli space. Since the fixed points are in one-to-one correspondence with the molten configurations of C_{Δ_*} , we can write the Witten index as a sum over the molten crystals \mathfrak{p} . The D2 and D0 charges for a given \mathfrak{p} are determined by $d_k := \dim M_k$ for $k \in Q_0$. This d_k is in fact the number of atoms in \mathfrak{p} which are associated with the k -th quiver node. To be more specific, let us define the generating function of the Witten index $\Omega(\gamma)$ as

$$\mathcal{Z}_{\text{BPS}} = \sum_{n, m^I \in \mathbb{Z}} \Omega(\mathcal{D} + m^I \beta_I - ndV) q^n \prod_I Q_I^{m^I}, \quad (2.8)$$

where q and Q_I are Boltzmann weights for D0 and D2 charges. The index I runs over $1, \dots, N$ where N is the number of the compact two-cycles in the Calabi-Yau three-fold Y_Σ . We also define the generating function of the molten crystals as

$$\mathcal{Z}_{\text{crystal}} = \sum_{\mathfrak{p}} (-1)^{\dim_{\mathbb{C}} \mathcal{M}_{\text{D6}}} \prod_{i \in Q_0} x_i^{d_i}, \quad (2.9)$$

where x_i is a Boltzmann weight for the i -th node in Q and \mathcal{M}_{D6} denotes the moduli space of the BPS states with charges $\{d_i\}$. The sign factor depends on the complex dimension of the moduli space \mathcal{M}_{D6} . Now, what was pointed out in [5] is that

$$\mathcal{Z}_{\text{BPS}} = \mathcal{Z}_{\text{crystal}} \quad (2.10)$$

holds under a suitable identification between the Boltzmann weights (q, Q_I) and x_i . The explicit identification between the Boltzmann weights depends on the original Calabi-Yau three-fold Y_Σ .

3 Crystal melting for D4-D2-D0 states

In this section, we replace the D6-brane with a non-compact D4-brane on a toric divisor and consider BPS D2-D0 states bound to the D4-brane. The main difference is that the flavor D4-brane gives an additional superpotential term which reduces the

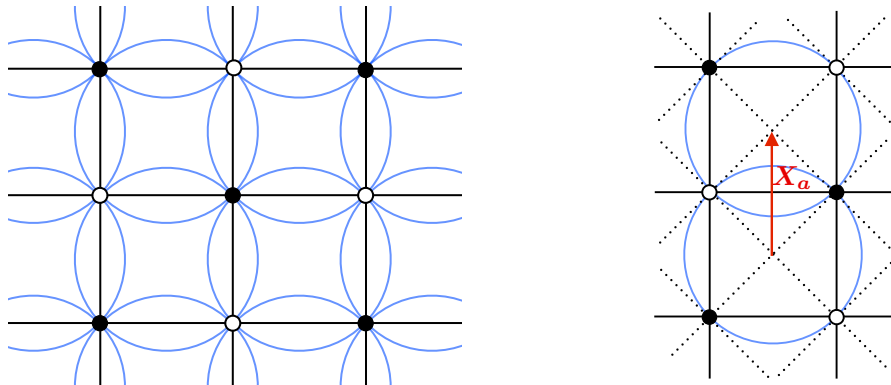


Figure 7: Left: An isoradial embedding of Q^\vee on T^2 , shown in its universal cover. Every vertex $f \in Q_0^\vee$ at the boundary of a face $k \in Q_2^\vee$ is on a unit circle c_k surrounding the face. Right: A Dimer model with an isoradial embedding implies a rhombus tiling of T^2 .

moduli space of the quiver quantum mechanics on the D-branes. We will show that the BPS index of the D4-D2-D0 states is evaluated by counting *two-dimensional* melting crystals. We particularly concentrate on dimer models with *isoradial embedding* as we explain in subsection 3.1.

3.1 Isoradial embedding

As reviewed in section 2, the brane tiling gives a dimer model Q^\vee associated with the toric Calabi-Yau three-fold Y_Σ . The universal cover \tilde{Q}^\vee of Q^\vee plays an essential role in the construction of the crystal melting model. In the rest of this paper, we particularly consider dimer models with *isoradial embedding*. The isoradial embedding is an embedding of Q^\vee in T^2 so that every vertex $f \in Q_0^\vee$ at the boundary of a face $k \in Q_2^\vee$ is on a unit circle c_k (right picture of figure 7). Dimer models with an isoradial embedding have been discussed in the study of R-charges in the IR superconformal fixed point [20]. The necessary and sufficient condition for Q^\vee to admit an isoradial embedding is reviewed in appendix B. What is important here is that the existence of a dimer model with an isoradial embedding was shown in [51] for an arbitrary toric Calabi-Yau three-fold.¹⁵ In the rest of this paper, we will focus on such a class of dimer models.

An important property of such dimer models is the existence of a rhombus tiling

¹⁵The authors thank Kazushi Ueda for pointing out this.

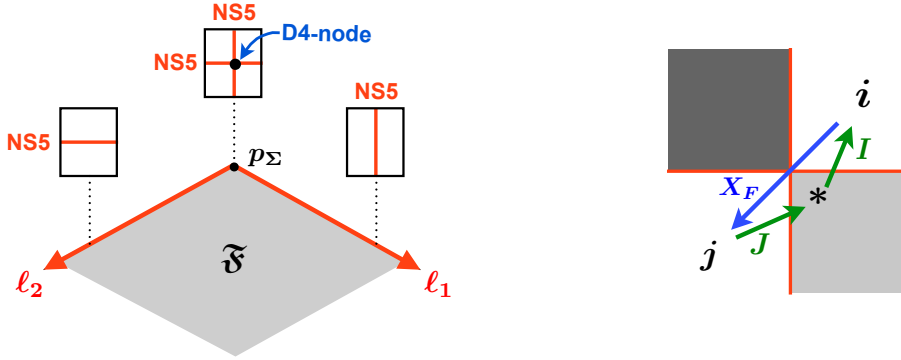


Figure 8: Left: After the T-dual transformations, the D4-brane becomes a flavor D2-brane filling up the facet \mathfrak{F} in the toric base, whose boundary is embedded in two NS5-branes along ℓ_1 and ℓ_2 . Right: In the brane tiling at p_Σ , the intersection point of the boundary NS5-branes is attached to two dynamical D2-branes i and j . The D4-node is located at the intersection, and induces two massless “quarks” I and J .

on T^2 . Given an isoradial embedding of Q^\vee , we can draw a line from a quiver vertex k to a dimer vertex f if f is on the unit circle c_k . Such lines form rhombi as in the right picture of figure 7. Note that each rhombus is associated with a chiral multiplet X_a . The fact that any dimer vertex is on some unit circle implies that this procedure leads to a rhombus tiling on T^2 . We will exploit this property heavily in the main part of this section.

3.2 Flavor D4-node

Let us now discuss the location of the flavor D4-brane in the brane tiling. We assume the D4-brane is wrapping on a toric divisor \mathcal{D} corresponding to a *corner* of the toric diagram Σ . The reason for this is that we want to make \mathcal{D} non-degenerate in the singular Calabi-Yau limit. The projection of \mathcal{D} to the toric base is a two-dimensional facet \mathfrak{F} bounded by two semi-infinite lines ℓ_1 and ℓ_2 . The lines ℓ_1, ℓ_2 are associated with two external legs of the toric web-diagram. The T-duality along T^2 maps the D4-brane to a flavor D2-brane filling up the facet \mathfrak{F} . The flavor D2-brane is bounded by two intersecting NS5-branes, each of which wraps on a one-cycle of T^2 and extends along ℓ_1 or ℓ_2 (figure 8). At the intersection point p_Σ of ℓ_1 and ℓ_2 , we have a brane tiling system as in figure 3. Note that the boundary of the flavor D2-brane is a point in T^2 and embedded in the boundary NS5-branes. In particular, in the brane tiling system

at p_Σ , the flavor D2-brane is located at the intersection point of the two boundary NS5-branes (figure 8), which gives a flavor “D4-node.” We use the same symbol $*$ to denote the D4-node in the quiver diagram, but it gives rise to quite different physics from the D6-node.

In the brane tiling, an intersection of two NS5-branes is always attached to two dynamical D2-branes (coming from the original D2-D0 states on Y_Σ). This implies that the D4-node has two massless “quarks” attached to it. To be more specific, suppose that the D4-node $*$ is adjacent to dynamical D2-branes i and j , and there is a chiral field X_F associated with an arrow from i to j (the right picture of figure 8). Then *we have a “quark” I associated with an arrow from $*$ to i as well as an “anti-quark” J associated with an arrow from j to $*$.* The quark and anti-quark are involved in the following additional superpotential term [23]:

$$W_{\text{flavor}} = JX_F I, \quad (3.1)$$

which gives additional F-term conditions

$$JX_F = 0, \quad X_F I = 0. \quad (3.2)$$

The total superpotential is now written as $W = W_0 + W_{\text{flavor}}$. The first term W_0 does not contain I, J , and can be read off from the brane tiling as explained in subsection 2.1. The additional potential (3.1) also modifies the F-term condition with respect to X_F as

$$\frac{\partial W_0}{\partial X_F} + IJ = 0. \quad (3.3)$$

Thus, we now have two different F-term constraints (3.2) and (3.3) from the D6-D2-D0 case. Both of them are induced by the additional superpotential (3.1). In the next subsection, we discuss how the two differences change the moduli space of supersymmetric vacua.

The location of the node i will be important in the construction of the two-dimensional crystal melting model. In fact, it gives a framing for the quiver representation. We stress here that i is the *starting node* of X_F .

We also mention that the boundary NS5-branes of the facet \mathfrak{F} in general have several intersections in T^2 . For example, when the Calabi-Yau is $\mathbb{C}^2/\mathbb{Z}_N \times \mathbb{C}$ and the D4-brane is on $\mathbb{C}^2/\mathbb{Z}_N$, there are N different intersection points of the boundary NS5-branes. In general, the D4-node is located at one of the intersection points, and the choice is related to the holonomy of the gauge field at infinity on the D4-brane. We will discuss this in more detail in subsection 4.4.

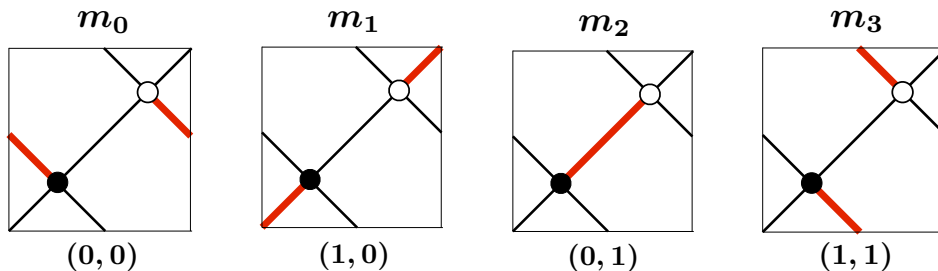


Figure 9: The possible perfect matchings in the case of conifold. Each perfect matching is associated with a lattice point of the toric diagram.

3.3 Moduli space of vacua

In this subsection, we study the moduli space \mathcal{M}_{D4} of the quiver quantum mechanics on the D4-D2-D0 state. The F-term conditions are now given by (3.2) and (3.3) together with

$$\frac{\partial W_0}{\partial X_a} = 0 \quad \text{for} \quad X_a \neq X_F. \quad (3.4)$$

We particularly show that the moduli space is a subspace of the moduli space \mathcal{M}_{D6} of the parent D6-D2-D0 state obtained by replacing the D4-brane with a D6-brane. The subspace is characterized by the invariance under the action of a $U(1)$ -subgroup of $U(1)^2 \times U(1)_R$. The $U(1)$ -subgroup depends on the divisor \mathcal{D} wrapped by the D4-brane.

Perfect matchings

To describe this, we first introduce so called “perfect matchings” of the bipartite graph Q^\vee . Every edge in Q_1^\vee has its definite orientation from black to white vertex. A perfect matching m is defined as a collection of such oriented edges in Q^\vee so that every vertex in Q_0^\vee is attached to one and only one edge in m . All perfect matchings in the conifold case are shown in figure 9. We then define the “slope” (h_x, h_y) of perfect matchings [18, 52]. We first fix a reference perfect matching m_0 and consider $m_\alpha - m_0$ for every perfect matching m_α , where the minus sign reverses the orientation of the edges.¹⁶ The edges in $m_\alpha - m_0$ always form a closed *oriented* curve in Q^\vee . When lifted to the

¹⁶To be more precise, we here regard m_α and m_0 as elements of a linear space over \mathbb{Z} which is generated by the edges in Q^\vee . For any edge e in Q^\vee , we identify $-e$ with the same edge of the opposite orientation. Then, for any two perfect matchings m_α and m_β , the element $m_\alpha - m_\beta$ can be identified with a closed oriented curve in Q^\vee , or in T^2 .

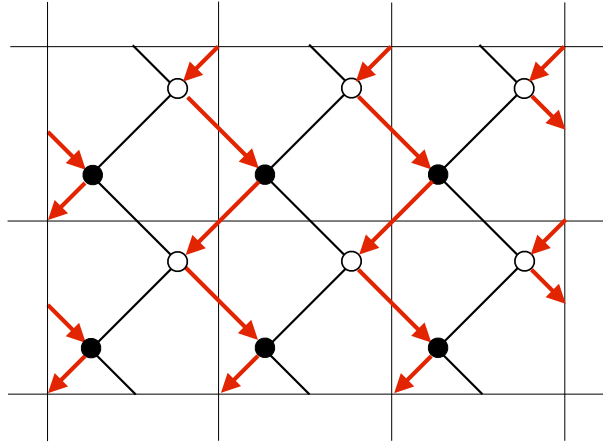


Figure 10: The uplift of $m_1 - m_0$ to the universal cover. The red arrows divide the universal cover into an infinite number of regions. The slopes are defined as the changes of the height function along the two periodic directions. This example has the slope $(1, 0)$.

universal cover \mathbb{R}^2 of T^2 , such a closed curve divides \mathbb{R}^2 into an infinite number of regions (figure 10). Then we define a height function on the universal cover, which takes a constant value in each region. We require that the height function changes by ± 1 when we move to an adjacent region crossing the curve. The sign of the height change depends on the orientation of the curve crossed. Then the *slope* (h_x, h_y) of m_α is defined by the height changes in the two periodic directions of the quotient $\mathbb{R}^2/\mathbb{Z}^2 \simeq T^2$ (figure 10).

What is striking here is that h_x, h_y give a *surjective* map from the perfect matchings to the lattice points of the toric diagram Σ , where (h_x, h_y) represents the relative positions of the lattice point [17, 18, 52]. For example, (h_x, h_y) for all the perfect matchings in the conifold case are shown in figure 9. Note that the ambiguity of the choice of the reference matching m_0 is absorbed by shifting the origin. Since the lattice points of Σ are in one-to-one correspondence with toric divisors, we also have a surjection φ from perfect matchings to toric divisors. Although φ is not necessarily bijective, a divisor \mathcal{D}' associated with a *corner* of the toric diagram has a unique perfect matching $m_{\mathcal{D}'}$ such that $\varphi(m_{\mathcal{D}'}) = \mathcal{D}'$ if the brane tiling admits an isoradial embedding [51, 24]. Since our divisor \mathcal{D} is associated with a corner of the toric diagram, we have a unique perfect matching $m_{\mathcal{D}}$.

Constraints on supersymmetric vacua

We now claim that there are two constraints on the field configuration at supersymmetric vacua, which are derived from the F- and D-term conditions. The first constraint is

$$J = 0, \tag{3.5}$$

which reduces (3.3) back to the original one $\partial W_0/\partial X_F = 0$. Although (3.5) can easily be proven at a torus fixed point of the moduli space, it in fact holds at any point of the moduli space of vacua. We will prove this in subsection 3.7. The second constraint is that for any chiral field $X_a \in Q_1$

$$X_a = 0 \quad \text{if} \quad \psi(X_a) \in m_{\mathcal{D}}. \tag{3.6}$$

Here, recall that $\psi : Q \rightarrow Q^\vee$ is a dual map. As we will see later, $\psi(X_F)$ is always included in the perfect matching $m_{\mathcal{D}}$. Therefore the condition (3.6) is generically stronger than (3.2). However, we claim that (3.6) follows from (3.2) if combined with the θ -stability for $\theta_k < 0, \theta_* \geq 0$ and the other F-term conditions. We will prove this in subsection 3.8.

Now, the two different F-term conditions (3.2) and (3.3) from the D6-D2-D0 cases are simplified; the former is replaced with (3.6) while the latter reduces back to the original one. Moreover, the ‘‘anti-quark’’ J , which does not exist in the D6-D2-D0 case, vanishes on supersymmetric vacua. *Hence, the moduli space \mathcal{M}_{D4} of the D4-D2-D0 state is obtained just by imposing (3.6) on the moduli space \mathcal{M}_{D6} of the parent D6-D2-D0 state. Here the parent D6-D2-D0 state is obtained by replacing the D4-brane with a D6-brane.* In other words, \mathcal{M}_{D4} is naturally regarded as a subspace of \mathcal{M}_{D6} . This reflects the fact that our D4-brane extends only in a divisor of the Calabi-Yau three-fold while the D6-brane wraps on the whole three-fold. The constraint (3.6) is interpreted to mean that $X_a \in \psi^{-1}(m_{\mathcal{D}})$ describes a fluctuation of the fractional branes in a transverse direction to the D4-brane world-volume. As described in appendix C, we can verify this interpretation by considering a single D0-probe.

From the mathematical point of view, our claim is the following. Let Q' be a new quiver such that $Q'_0 = \widehat{Q}_0 = Q_0 \cup \{*\}$ and $Q'_1 = \widehat{Q}_1 \cup \{J\} = Q_1 \cup \{I, J\}$. Let us define \mathcal{F}' to be the ideal of $\mathbb{C}Q'$ generated by $\partial W/\partial I, \partial W/\partial J$ and $\partial W/\partial X_a$ for all $X_a \in Q_1$.¹⁷ We then define

$$A' := \mathbb{C}Q'/\mathcal{F}'. \tag{3.7}$$

¹⁷Recall that $W = W_0 + W_{\text{flavor}}$.

We also define an another algebra

$$\mathring{A} := \mathbb{C}\widehat{Q}/\mathring{\mathcal{F}}, \quad (3.8)$$

where $\mathring{\mathcal{F}}$ is the ideal of $\mathbb{C}\widehat{Q}$ generated by all the $\partial W_0/\partial X_a$ and X_b such that $\psi(X_b) \in m_{\mathcal{D}}$. Note that, since $\psi(X_F) \in m_{\mathcal{D}}$, we have $[X_F] = 0$ in \mathring{A} .¹⁸ Setting $X_F = 0$ implies $\partial W/\partial I = \partial W/\partial J = 0$ and $\partial W/\partial X_a = \partial W_0/\partial X_a$ in $\mathbb{C}Q'$. Therefore an \mathring{A} -module is naturally regarded as an A' -module. However, the converse is not always true. Now, our claim is that there is a one-to-one correspondence between θ -stable A' -modules and θ -stable \mathring{A} -modules if we take θ_k, θ_* so that $\theta_k < 0$ and $\theta_* \geq 0$. We will prove this in subsections 3.7 and 3.8.

\mathcal{M}_{D4} in \mathcal{M}_{D6}

We here show that \mathcal{M}_{D4} as a subspace of \mathcal{M}_{D6} is characterized by its invariance under a $U(1)$ -subgroup of $U(1)^2 \times U(1)_R \simeq U(1)^3$. To see this, let us consider $t \in T$ such that

$$t(X_a) = \begin{cases} e^{i\alpha} & \text{if } \psi(X_a) \in m_{\mathcal{D}} \\ 1 & \text{if } \psi(X_a) \notin m_{\mathcal{D}} \end{cases}, \quad (3.9)$$

for $\alpha \in \mathbb{R}$. Since $m_{\mathcal{D}}$ is a perfect matching of Q^\vee , this t preserves all the F-term conditions for the parent D6-D2-D0 state. Furthermore, for general α , this t -action cannot be absorbed into gauge transformations. In fact, since each superpotential term includes one and only one chiral field involved in $m_{\mathcal{D}}$, the t -action (3.9) does *not* preserve the superpotential. Such a $U(1)$ -action cannot be absorbed by gauge $U(1)^{|Q_0|-1}$. Therefore, the t -actions (3.9) form a $U(1)$ -subgroup of $U(1)^3$ acting on \mathcal{M}_{D6} . We denote this by $U(1)_{m_{\mathcal{D}}}$.

Since all chiral fields involved in $m_{\mathcal{D}}$ vanish on \mathcal{M}_{D4} , the moduli space \mathcal{M}_{D4} is invariant under the action of $U(1)_{m_{\mathcal{D}}}$. Thus $U(1)^3$ reduces to $U(1)^2 \simeq U(1)^3/U(1)_{m_{\mathcal{D}}}$ on \mathcal{M}_{D4} . The Witten index of the quiver quantum mechanics is then, up to sign, the number of $U(1)^2$ -fixed points of \mathcal{M}_{D4} . Since the perfect matching $m_{\mathcal{D}}$ depends on the divisor \mathcal{D} wrapped by the D4-brane, so does the residual $U(1)^2$. Note that all these properties of \mathcal{M}_{D4} essentially follow from the constraints (3.6) and (3.5). We will derive them in subsections 3.8 and 3.7.

Let us here mention that the relation between \mathcal{M}_{D4} and \mathcal{M}_{D6} is quite similar to that between the instanton and vortex moduli spaces. The moduli space of vortices

¹⁸Here, $[X_F]$ is the equivalence class of X_F .

in $d = 2, \mathcal{N} = (4, 4)$ theories was studied in [53] and shown to be embedded in the moduli space of instantons.¹⁹ Moreover, it was pointed out that the vortex moduli space can be regarded as a $U(1)$ invariant subspace of the instanton moduli space. It would be interesting to study this similarity further.

3.4 Two-dimensional melting crystal

We now consider the $U(1)^2$ -fixed points of the moduli space \mathcal{M}_{D_4} . The inclusion map $\mathfrak{i} : \mathcal{M}_{D_4} \hookrightarrow \mathcal{M}_{D_6}$ implies that they are naturally regarded as some $U(1)^3$ -fixed points of \mathcal{M}_{D_6} . In other words, we are interested in a class of $U(1)^3$ -fixed points of \mathcal{M}_{D_6} which are included in $\mathfrak{i}(\mathcal{M}_{D_4})$. Recall here that any $U(1)^3$ -fixed points of \mathcal{M}_{D_6} is expressed by a finite ideal π of Δ_* , where Δ_* is the F-term equivalence class of paths starting at $*$. In particular, the elements of π form the basis of the corresponding module. Now, what kind of finite ideal corresponds to a fixed point in $\mathfrak{i}(\mathcal{M}_{D_4})$? The projection of \mathcal{M}_{D_6} to $\mathfrak{i}(\mathcal{M}_{D_4})$ is given by (3.6), which eliminates all the paths crossing the perfect matching $m_{\mathcal{D}}$. Let us define $\mathring{\Delta}_*$ as the set of F-term equivalence classes of paths which do *not* cross the perfect matching $m_{\mathcal{D}}$. By definition, $\mathring{\Delta}_*$ is a subset of Δ_* . It is now clear that the $U(1)^3$ -fixed points in $\mathfrak{i}(\mathcal{M}_{D_4})$, or equivalently the $U(1)^2$ -fixed points of \mathcal{M}_{D_4} , are in one-to-one correspondence with finite ideals of $\mathring{\Delta}_*$. From the mathematical viewpoint, we find that $U(1)^2$ -invariant θ -stable \mathring{A} -modules are in one-to-one correspondence with finite ideals of $\mathring{\Delta}_*$.

Next, recall that $f : \Delta_* \rightarrow C_{\Delta_*}$ is a bijection from Δ_* to a three-dimensional crystal C_{Δ_*} , where $[v_k \omega^\ell] \in \Delta_*$ is mapped to an atom on the node $k \in \tilde{Q}_0$ at the depth ℓ . Note that we here fix a reference node in \tilde{Q}_0 and assume that the flavor-brane node $*$ is attached to it; there is a quark I from $*$ to the node. We denote by \tilde{i} the reference node because it is an uplift of $i \in Q_0$. Let us now define $C_{\mathring{\Delta}_*} := f(\mathring{\Delta}_*)$, which is a subcrystal of C_{Δ_*} . We call $C_{\mathring{\Delta}_*}$ “reduced crystal.” The finite ideals of $\mathring{\Delta}_*$ are then in one-to-one correspondence with molten configurations of $C_{\mathring{\Delta}_*}$. The melting rule is the same as before; For a molten configuration \mathfrak{p} of $C_{\mathring{\Delta}_*}$,

$$\text{a bond from } \beta \in C_{\mathring{\Delta}_*} \text{ to } \alpha \in \mathfrak{p} \text{ implies } \beta \in \mathfrak{p}.$$

Note here that if one representative path of $[v_k \omega^\ell] \in \Delta_*$ includes some chiral field in $\psi^{-1}(m_{\mathcal{D}})$ then so does any other representative path of $[v_k \omega^\ell]$. This implies that *the*

¹⁹See also [54, 55, 56] for the localization on the vortex moduli space of $d = 2, \mathcal{N} = (2, 2)$ theories.

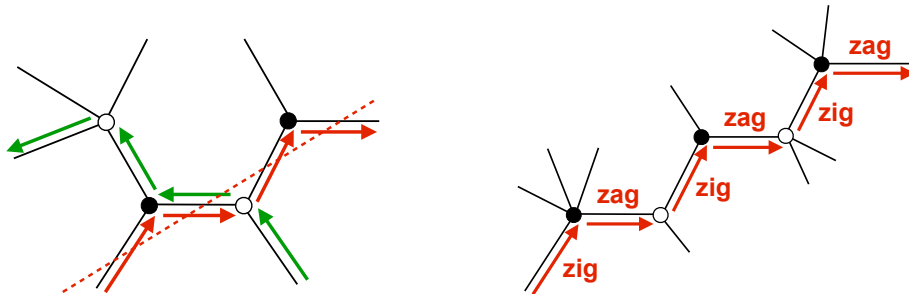


Figure 11: Left: Two examples of zig-zag paths. In general, an edge in Q^\vee is involved in two different zig-zag paths. There is a one-to-one correspondence between zig-zag paths and NS5-branes. For example, the red dotted line describes a NS5-brane associated with the red zig-zag path. Right: A zig-zag path \mathcal{P} is decomposed into $\text{Zig}(\mathcal{P})$ and $\text{Zag}(\mathcal{P})$.

reduced crystal $C_{\overset{\circ}{\Delta}_*}$ is obtained from the original crystal C_{Δ_*} by eliminating all the bonds associated with chiral fields involved in $m_{\mathcal{D}}$.

Now, let us consider how the reduced crystal is embedded in the original three-dimensional crystal. For any element $[v_k \omega^\ell] \in \overset{\circ}{\Delta}_*$, its representative path $v_k \omega^\ell$ cannot contain any chiral field in $\psi^{-1}(m_{\mathcal{D}})$. However, ω includes one such chiral field. Thus we always have $\ell = 0$, namely any element of $\overset{\circ}{\Delta}_*$ is represented by a shortest path from $*$. This particularly implies that *the reduced crystal $C_{\overset{\circ}{\Delta}_*}$ lies in a two-dimensional plane at the depth zero.*

3.5 Shape of the crystal

We have seen that the reduced crystal is always a two-dimensional crystal. We now discuss the precise shape of the crystal. Let us first introduce so-called ‘‘zig-zag paths.’’ A zig-zag path is an oriented path in Q^\vee which satisfies the following property: along a zig-zag path, we turn maximally right at a black vertex as well as maximally left at a white vertex (figure 11). This property is exactly the same as the property of cycles wrapped by NS5-branes in the brane tiling. In fact, there is a bijection from the NS5-branes to the zig-zag paths of Q^\vee , which preserves the winding numbers. This also implies a one-to-one map between the zig-zag paths and the external legs of the toric web-diagram. The zig-zag paths of a dimer model with an isoradial embedding have some nice properties as described in appendix B. In particular, when lifted to the universal cover \tilde{Q}^\vee , any two zig-zag paths share at most one edge.

Since a zig-zag path \mathcal{P} is oriented, all the edges in \mathcal{P} are also oriented. We then define $\text{Zig}(\mathcal{P})$ as a collection of edges in \mathcal{P} which are from *white to black* vertex. We also define $\text{Zag}(\mathcal{P}) := \mathcal{P} - \text{Zig}(\mathcal{P})$ (the right picture of figure 11). Now, recall that our flavor brane is bounded by two NS5-branes at ℓ_1, ℓ_2 . They are associated with two zig-zag paths in Q^\vee , which we denote by \mathcal{P}_1 and \mathcal{P}_2 respectively. The winding numbers of $\mathcal{P}_1, \mathcal{P}_2$ are determined by the directions of ℓ_1, ℓ_2 . Then it was shown in [24] that

$$\text{Zig}(\mathcal{P}_1), \text{Zag}(\mathcal{P}_2) \subset m_{\mathcal{D}}. \quad (3.10)$$

Note that, since \mathcal{P}_1 and \mathcal{P}_2 have different winding numbers, they always intersect with each other on Q^\vee . At each intersection of \mathcal{P}_1 and \mathcal{P}_2 , they share an edge $\psi(Y)$ for some chiral multiplet $Y \in Q_1$. Due to the condition (3.10), such a chiral multiplet Y always satisfies

$$\psi(Y) \in \text{Zig}(\mathcal{P}_1) \cap \text{Zag}(\mathcal{P}_2) \subset m_{\mathcal{D}}. \quad (3.11)$$

Note that X_F defined in subsection 3.2 is one such chiral multiplet. Therefore we always have $\psi(X_F) \in m_{\mathcal{D}}$.

Let us now consider the uplifts of $\mathcal{P}_1, \mathcal{P}_2$ to the universal cover \tilde{Q}^\vee , where we have a natural projection $p^\vee : \tilde{Q}^\vee \rightarrow Q^\vee$. Recall that there is a reference node \tilde{i} in $\tilde{Q}_0 \simeq \tilde{Q}_2^\vee$ which is attached to the D4-node $*$. The node \tilde{i} is also attached to a lift of the chiral multiplet X_F , which we denote by \tilde{X}_F (figure 12). Let $\tilde{\psi} : \tilde{Q} \rightarrow \tilde{Q}^\vee$ be the dual map on the universal cover. There are two zig-zag paths of \tilde{Q}^\vee which share the edge $\tilde{\psi}(\tilde{X}_F)$ at their intersection. When projected to Q^\vee , they map to \mathcal{P}_1 and \mathcal{P}_2 . We therefore denote them by $\tilde{\mathcal{P}}_1$ and $\tilde{\mathcal{P}}_2$, respectively. The two zig-zag paths $\tilde{\mathcal{P}}_1, \tilde{\mathcal{P}}_2$ divide the universal cover of T^2 into four regions. We denote one of them which includes \tilde{i} by \mathfrak{R} . See figure 12 for example in the conifold case, where the blue face is \tilde{i} and the orange region including \tilde{i} is \mathfrak{R} .

What we want to show is that the reduced crystal $C_{\Delta_*}^\circ$ fills up the region \mathfrak{R} and $\tilde{\mathcal{P}}_1, \tilde{\mathcal{P}}_2$ give the boundary of the crystal. Here, since $C_{\Delta_*}^\circ$ lies at the depth zero, we identify atoms in $C_{\Delta_*}^\circ$ with faces in \tilde{Q}^\vee . Recall first that $\tilde{\mathcal{P}}_1$ and $\tilde{\mathcal{P}}_2$ share $\tilde{\psi}(\tilde{X}_F)$ at their intersection. The fact $\psi(X_F) \in \text{Zig}(\mathcal{P}_1) \cap \text{Zag}(\mathcal{P}_2)$ then implies that \tilde{X}_F is always an *out-going* arrow from \mathfrak{R} and eliminated by the constraint (3.6).²⁰ From this and

²⁰Recall that our chiral multiplets have their definite orientations such that they encircle black (white) vertices in Q^\vee clockwise (counter-clockwise).

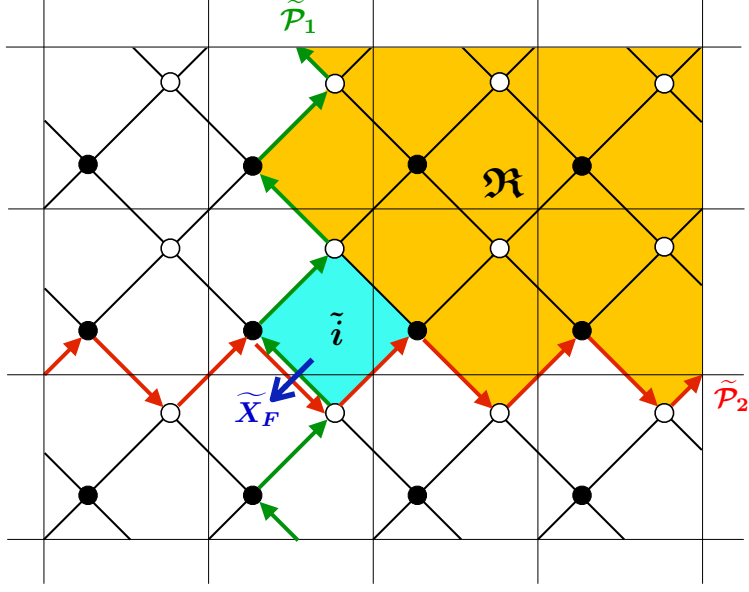


Figure 12: The periodic dimer model \tilde{Q}^\vee in the conifold case. The two zig-zag paths $\tilde{\mathcal{P}}_1$ and $\tilde{\mathcal{P}}_2$ divide the universal cover of T^2 into four regions. We denote by \mathfrak{R} a region including the face \tilde{i} . We here assume that \mathcal{D} is associated with the upper-right corner of the toric diagram in figure 2.

(3.10), it follows that *all the out-going arrows from \mathfrak{R} is eliminated by (3.6)*. This means that the reduced crystal C_{Δ_*} is inside the region \mathfrak{R} .

Furthermore, if $\ell \in \tilde{Q}_0 \simeq \tilde{Q}_2^\vee$ is inside \mathfrak{R} , then the reduced crystal C_{Δ_*} always includes an atom placed on ℓ . This can be shown as follows. Let us fix $k, \ell \in \tilde{Q}_0$ and consider all the zig-zag paths of \tilde{Q}^\vee which have k on its right side and ℓ on its left side. Such zig-zag paths are associated with some external legs of the toric web-diagram. We define C_- as a cone generated by such external legs. We also consider all the zig-zag paths on \tilde{Q}^\vee which has k on its left side and ℓ on its right side, and define C_+ similarly. Then, it was shown in [24] that if the cone associated with our divisor \mathcal{D} is located in the clockwise direction of C_+ and in the counter-clockwise direction of C_- , as in figure 13, then there is always a path from k to ℓ which does not cross $(p^\vee)^{-1}(m_{\mathcal{D}})$.²¹ When we set $k = \tilde{i}$ and ℓ to be inside \mathfrak{R} , then the cone associated with \mathcal{D} is always in the clockwise direction of C_+ and in the counter-clockwise direction of C_- . Therefore, there is always a path from \tilde{i} to $\ell \in \tilde{Q}_0$ without crossing $(p^\vee)^{-1}(m_{\mathcal{D}})$.

²¹Here $(p^\vee)^{-1}(m_{\mathcal{D}})$ is the inverse image of $m_{\mathcal{D}}$ through $p^\vee : \tilde{Q}^\vee \rightarrow Q^\vee$, and itself is a perfect matching of \tilde{Q}^\vee .

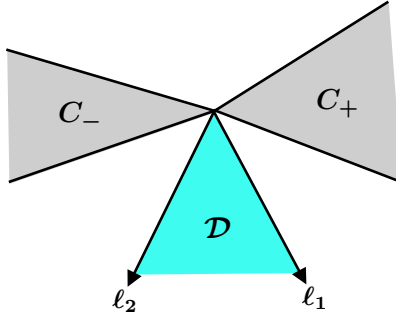


Figure 13: If the cone associated with our divisor \mathcal{D} is in the clockwise side of C_+ and in the counter-clockwise side of C_- , then there is a path from k to ℓ without crossing $(p^\vee)^{-1}(m_{\mathcal{D}})$.

This means that $C_{\Delta_*}^\circ$ includes an atom placed on ℓ . Since ℓ is an arbitrary node in \mathfrak{R} , this implies that the reduced crystal $C_{\Delta_*}^\circ$ fills up the region \mathfrak{R} .

3.6 Partition function

We have shown that $U(1)^2$ -fixed points of the moduli space \mathcal{M}_{D4} are in one-to-one correspondence with molten configurations of the reduced crystal $C_{\Delta_*}^\circ$ lying in \mathfrak{R} . Then the partition function of the BPS D4-D2-D0 states is given by

$$\mathcal{Z}_{D4-D2-D0} = \sum_{\mathfrak{p}} (-1)^{\dim_{\mathbb{C}}(\mathcal{M}_{\vec{d}})} \prod_{k \in Q_0} x_k^{d_k}, \quad (3.12)$$

where \mathfrak{p} runs over all possible molten configurations of $C_{\Delta_*}^\circ$ and d_i is the number of i -th atoms in \mathfrak{p} . We denote by $\mathcal{M}_{\vec{d}}$ the moduli space of BPS states with charge $\{d_k\}$, or equivalently the moduli space of vacua of the quiver quantum mechanics with ranks $\{d_k\}$ of the gauge groups.

In general, the complex dimension of the moduli space $\dim_{\mathbb{C}}(\mathcal{M}_{\vec{d}})$ is calculated as

$$\dim_{\mathbb{C}}(\mathcal{M}_{\vec{d}}) = n_1 - n_2 - n_3, \quad (3.13)$$

where n_1 is the degrees of freedom of chiral fields which do not involved in the perfect matching $m_{\mathcal{D}}$, and n_2 is the number of non-trivial F-term conditions. In general n_1 can be written as

$$n_1 = \sum_{X \notin m_{\mathcal{D}}} d_{s(X)} d_{t(X)}, \quad (3.14)$$

where $s(X)$ and $t(X)$ is the starting and ending node of a chiral field $X \in \widehat{Q}_1$, respectively. The third term in (3.13) is given by

$$n_3 = \sum_{k \in Q_0} (d_k)^2, \quad (3.15)$$

which is the number of gauge degrees of freedom. Note that our gauge group has already been complexified to be $\prod_{k \in Q_0} GL(d_k)$, as explained in subsection 2.3.

In the next section, we describe some examples and show that our construction perfectly reproduces known statistical models for D4-D2-D0 states on \mathbb{C}^3 , (generalized) conifold, and $\mathbb{C}^2/\mathbb{Z}_N \times \mathbb{C}$. We will also describe some examples of D4-D2-D0 crystal which have not been in the literature to the best of our knowledge.

3.7 Proof of $J = 0$

We here show that $J = 0$ follows on a θ -stable module with $\theta_k < 0$ for $k \in Q_0$. Since such a θ -stable module is a cyclic module generated by $\mathbf{m} \in M_*$, it is sufficient to show that

$$JvI = 0 \quad (3.16)$$

for any path v in Q . We assume that v is a path from i to j because otherwise (3.16) trivially holds. In general v can contain I and/or J . However, since I and J appear only as IJ in v , it is sufficient to consider v without including I, J .

Hereafter, we consider the universal cover \widetilde{Q} of Q and regard v as a path in \widetilde{Q} . We respectively denote by \tilde{i} and \tilde{j} the starting and the ending nodes of v in \widetilde{Q} , which are of course the uplifts of i and j . Now, for our purpose, it is sufficient to assume v is a shortest path from \tilde{i} to \tilde{j} . To see this, let us recall that our F-term equivalences are

$$\frac{\partial W_0}{\partial X_F} + IJ = 0, \quad \frac{\partial W_0}{\partial X_a} = 0 \quad (\text{for } X_a \neq X_F), \quad (3.17)$$

together with $X_F I = 0$ and $J X_F = 0$. If $J = 0$, these imply that v has a standard expression of the form [4]

$$v = v_0 \omega^{\ell_0}. \quad (3.18)$$

Here v_0 is a shortest path from \tilde{i} to \tilde{j} , ω is a loop which starts with X_F and surrounds a face in \widetilde{Q}_2 , and ℓ_0 is a non-negative integer. If J is non-vanishing, this expression is generally modified as

$$v = v_0 \omega^{\ell_0} + w_1 (IJ) v_1 \omega^{\ell_1} + \cdots + w_n (IJ) v_n \omega^{\ell_n}, \quad (3.19)$$

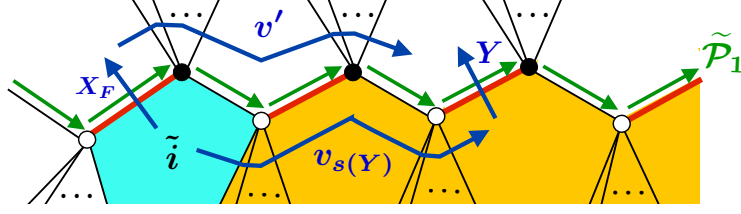


Figure 14: A shortest path $v_{s(Y)}$ from i to $s(Y)$ for an out-going arrow Y from \mathfrak{R} . Since Y crosses one of the red edges, there is a path v' such that $Yv_{s(Y)}$ is F-term equivalent to $v'X_F$.

where $\{v_a\}$ are shortest paths from \tilde{i} , and w_a are paths to \tilde{j} which are not necessarily shortest. Here, by shortest path, we mean a path which cannot be decomposed further as (3.19). Since ωI starts with $X_F I = 0$, the terms with $\ell_a \neq 0$ do not contribute to JvI . On the other hand, the terms with $\ell_a = 0$ contribute $Jw_a I Jv_a I$ to JvI . Therefore, if $JvI = 0$ is satisfied for all shortest paths v then it also holds for any other non-shortest paths v .

Let us now show that a shortest path v which gets outside the region \mathfrak{R} gives a vanishing contribution to JvI . Recall that any out-going arrow Y from \mathfrak{R} is an element of $\text{Zig}(\tilde{\mathcal{P}}_1) \cup \text{Zag}(\tilde{\mathcal{P}}_2)$. If v contains any such Y , then vI starts with $Yv_{s(Y)}I$ where $v_{s(Y)}$ is a shortest path from \tilde{i} to the starting node $s(Y)$ of Y (figure 14). However, since there is always a path v' such that $v'X_F$ is F-term equivalent to $Yv_{s(Y)}$, we find $Yv_{s(Y)}I = v'X_F I = 0$. Thus, if a shortest path v contains some out-going arrow from \mathfrak{R} then $JvI = 0$.

The remaining task is to show (3.16) for shortest paths v which are inside the region \mathfrak{R} . We first show the following lemma:

Lemma

A shortest path v from \tilde{i} to $k \in \tilde{Q}_0$ does not cross $(p^\vee)^{-1}(m_{\mathcal{D}})$ if k is inside \mathfrak{R} .

Proof. As mentioned in subsection 3.5, for any node $k \in \tilde{Q}_0$ inside \mathfrak{R} , there is a path v from \tilde{i} to k which does not cross $(p^\vee)^{-1}(m_{\mathcal{D}})$. This path is, in fact, a shortest path from \tilde{i} to k . The reason for this is that any non-shortest path contain at least one ω around some face in \tilde{Q}_2 , and therefore crosses $(p^\vee)^{-1}(m_{\mathcal{D}})$ at least once. \square

This lemma particularly implies that a shortest path v from \tilde{i} does not contain any

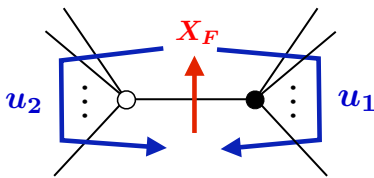


Figure 15: The relative sign in (3.21) implies $u_1 X_F$ surrounds a black node while $u_2 X_F$ surrounds a white node in \tilde{Q}^\vee .

X_F if v is inside \mathfrak{R} . We now assume that v is such a shortest path. We rewrite JvI as

$$JvI = \text{tr}(IJv) = -\text{tr}\left(\frac{\partial W_0}{\partial X_F} v\right) = \text{tr}(u_1 v) - \text{tr}(u_2 v), \quad (3.20)$$

where u_1 and u_2 are paths in Q such that

$$\frac{\partial W_0}{\partial X_F} = -u_1 + u_2. \quad (3.21)$$

The relative sign implies that $u_1 X_F$ surrounds a black node in \tilde{Q}_0^\vee while $u_2 X_F$ surrounds a white node (figure 15). Note that $u_1 v$ and $u_2 v$ form loops in Q , which we denote by L_1 and L_2 respectively. In terms of these, we can rewrite (3.20) as

$$JvI = \text{tr}(L_1) - \text{tr}(L_2). \quad (3.22)$$

In the rest of this subsection, we will show that this vanishes for any shortest path v inside \mathfrak{R} .

Rhombus tiling and F-term equivalence

Note that the two loops L_1, L_2 have the same winding number (n_x, n_y) . Since v is inside the region \mathfrak{R} , (n_x, n_y) always lies in a convex cone $\mathcal{C}_{\mathcal{D}}$ in \mathbb{R}^2 . The cone is naturally identified with \mathfrak{F} defined in subsection 3.2 and therefore depends on the choice of \mathcal{D} . We can generally write the winding number as

$$(n_x, n_y) = r(\hat{n}_x, \hat{n}_y), \quad (3.23)$$

where r is a positive integer and \hat{n}_x, \hat{n}_y are mutually prime integers. Since r depends on the shortest path v , we sometimes write it as r_v .

Recall here that there is a one-to-one correspondence between zig-zag paths and the external legs of the toric web-diagram. In particular, if there is a zig-zag path whose winding number is (n'_x, n'_y) then there is an external leg spanned by the vector

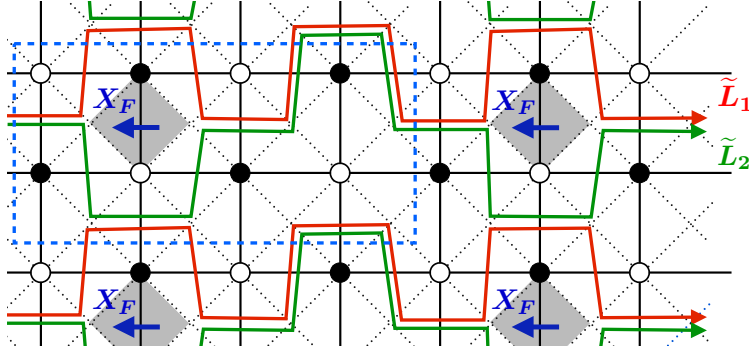


Figure 16: The situation in the case of $r = 1$. The blue dashed rectangle expresses the fundamental domain for the torus $\mathbb{R}^2/\mathbb{Z}^2$. The black solid edges together with the white and black nodes form the periodic dimer model \tilde{Q}^\vee . The union of the gray rhombi is denoted by \tilde{H}_F . When we regard \tilde{L}_1, \tilde{L}_2 as paths in \mathbb{R}^2 , they are continuously deformed into each other without crossing \tilde{H}_F .

(n'_x, n'_y) . Since \mathfrak{F} is a cone spanned by two adjacent external legs ℓ_1, ℓ_2 , the only zig-zag paths whose winding number lies in \mathcal{C}_D are \mathcal{P}_1 and \mathcal{P}_2 . This fact will be important in the proof of $\text{tr}(L_1) - \text{tr}(L_2) = 0$.

The case $r = 1$

We first consider the case $r = 1$. We will show that L_1 and L_2 are F-term equivalent to each other, which implies (3.22) vanishes. Recall that our brane tiling admits an isoradial embedding, and therefore we have a rhombus tiling on T^2 . We denote by H_F a rhombus including the chiral multiplet X_F . What is important here is that, when we regard L_1, L_2 as cycles of T^2 rather than those of Q , they can be continuously deformed into each other without crossing H_F . To see this, we move to the universal cover \mathbb{R}^2 . The uplifts of L_1, L_2 are paths with infinite length, which we denote by \tilde{L}_1 and \tilde{L}_2 respectively. Note that each of \tilde{L}_1, \tilde{L}_2 has an infinite number of connected components, which are just copies of one connected line with infinite length. Since v is a shortest path in \tilde{Q} , they have no self-intersection. The uplift of the rhombus H_F is an infinite number of rhombi. We denote by \tilde{H}_F the union of all such rhombi in \mathbb{R}^2 . We now see that \tilde{L}_1 can be continuously deformed into \tilde{L}_2 without crossing \tilde{H}_F (figure 16). This always follows when $r = 1$. Furthermore, we can perform this deformation periodically so that \tilde{L}_1 remains the uplift of some cycle of T^2 . This implies that, on T^2 , L_1 can be deformed into L_2 without crossing H_F .

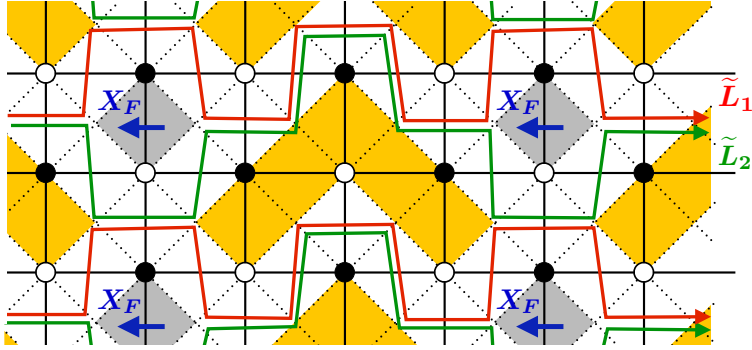


Figure 17: The collection of rhombi passed by \tilde{L}_1, \tilde{L}_2 (white rhombi) divides the universal cover into an infinite number of connected regions. The union of the regions which do not contain any X_F is denoted by τ . In this picture, τ is the union of the orange rhombi.

Note that this does *not* immediately mean L_1 and L_2 are F-term equivalent. When we regard them as paths in Q , rather than those in T^2 , we can deform them only by F-term equivalence. In fact, in a general dimer model, there could exist two homotopic paths which are not F-term equivalent to each other. However, there is a nice theorem that any two homotopic paths are F-term equivalent if the dimer model admits an isoradial embedding [57]. Below, we will generalize this and show that L_1 and L_2 are in fact F-term equivalent.

In the universal cover \mathbb{R}^2 , there are special rhombi which are passed by \tilde{L}_1 or \tilde{L}_2 . The collection of such rhombi divides \mathbb{R}^2 into an infinite number of connected regions. We denote by τ the union of the regions which do *not* contain any X_F (figure 17). Note that the boundary of τ has two kinds of vertices; quiver vertices and dimer vertices. Let us now consider to reduce the region τ via the F-term equivalence. We deform \tilde{L}_1 by using the F-term equivalence at the boundary of τ , which reduces the area of τ (figure 18). Reducing τ is possible only when the boundary of τ has a dimer vertex which is *not* attached to any rhombus edge lying *inside* τ [57]. We perform this deformation of \tilde{L}_1 *periodically* so that it is an uplift of a deformation of L_1 . Then this does not change the winding number of \tilde{L}_1 . We repeat this deformation and stop if we cannot reduce τ further. There are, in fact, only three possibilities to stop. The first possibility is that τ is empty when we stop. In this case \tilde{L}_1 coincides with \tilde{L}_2 after the operations, and therefore we find that L_1 is F-term equivalent to L_2 . The second possibility is that, when we stop, τ is not empty but can be written as the disjoint union of compact

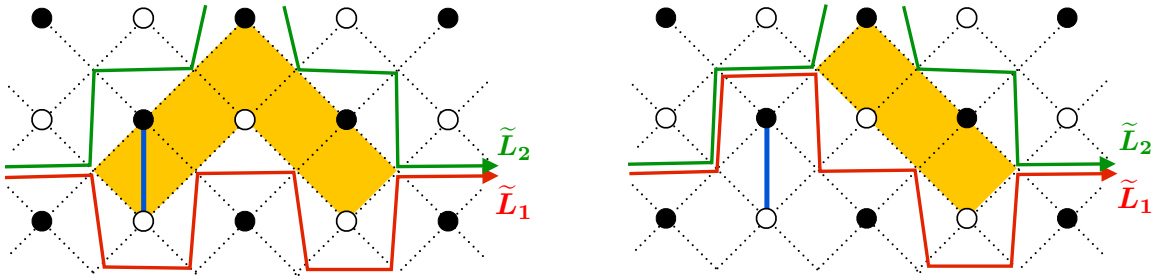


Figure 18: By using the F-term equivalence at the boundary of the region τ , we can reduce the area of τ . We here used the F-term condition associated with the blue edge. Reducing τ is possible only when we have a dimer vertex at the boundary of τ which is not attached to any rhombus edge lying *inside* τ .

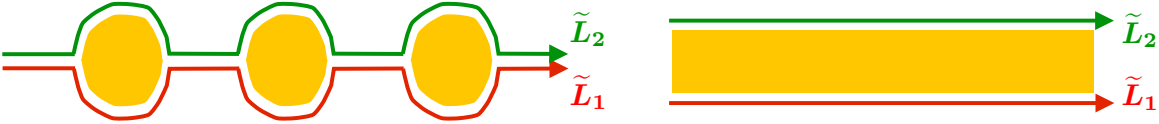


Figure 19: Left: The second possibility to stop. When we stop, the region τ is not empty but written as the disjoint union of compact regions. Right: The third possibility to stop. When we stop, τ is not empty and cannot be written as the disjoint union of compact regions.

regions. In this case, we have the situation illustrated in the left picture of figure 19. However, this is inconsistent with the rhombus tiling of \mathbb{R}^2 , which follows from Lemma 5.3.1 of [57]. Thus, the second possibility is forbidden. The third possibility is that, when we stop, τ is not empty and cannot be written as the disjoint union of compact regions. In this case, we have the situation as in the right picture of figure 19. This does not contradict with the lemma in [57], but still turns out to contradict with the rhombus tiling of \mathbb{R}^2 . To see this, note first that any dimer vertex at the boundary of τ is now attached to at least one rhombus edge lying inside τ , because otherwise we can further reduce τ . It also follows that any quiver vertex at the boundary of τ is attached to at least one such rhombus edge. Therefore the simplest case is that, at the boundary of τ , each (quiver or dimer) vertex is attached to only one edge lying inside τ . In this case, there is always a zig-zag path $\tilde{\mathcal{P}}$ included in the region τ (figure 20). When projected to T^2 , $\tilde{\mathcal{P}}$ is mapped to a zig-zag path of Q whose winding number is (n_x, n_y) . Since (n_x, n_y) lies in the convex cone $\mathcal{C}_{\mathcal{D}}$, such a zig-zag path should be \mathcal{P}_1

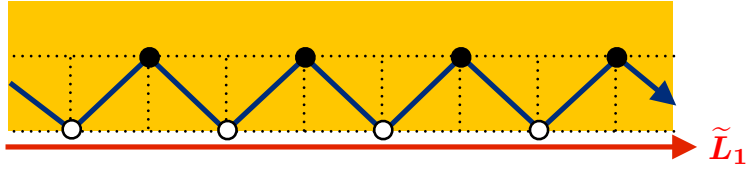


Figure 20: The simplest case of the third possibility. There is a zig-zag path inside \mathfrak{r} (blue path) which has the same winding number as L_1 . In this situation, we cannot deform \tilde{L}_1 to reduce \mathfrak{r} because every white dimer vertex at the boundary is attached to some rhombus edge lying inside \mathfrak{r} .

or \mathcal{P}_2 . Recall that both \mathcal{P}_1 and \mathcal{P}_2 involve X_F . Therefore $\tilde{\mathcal{P}}$ also involves X_F . This, however, contradicts with the fact that the region \mathfrak{r} does not contain any X_F . Hence, the simplest case does not occur. Let us then consider a non-simplest case. Namely, suppose that the boundary of \mathfrak{r} includes a vertex attached to more than one rhombus edge lying inside \mathfrak{r} . In this case, \tilde{L}_1 has to intersect with itself in order to be periodic in \mathbb{R}^2 . The periodicity of \tilde{L}_1 is necessary because it is the uplift of L_1 . However, the self-intersection of \tilde{L}_1 contradicts with the fact that v is a shortest path in \tilde{Q} . This implies that not only the second possibility but also the third possibility is forbidden. Hence, L_1 is always F-term equivalent to L_2 , which implies (3.22) vanishes.

The case $r \geq 2$

Next, we turn to the cases $r \geq 2$. In this case, $JvI = 0$ follows by induction on r . Since r depends on v , we here write it as r_v . We assume $Jv'I = 0$ for any v' with $r_{v'} < r_v$, and prove $JvI = 0$.

Note first that, in the case $r_v \geq 2$, it is not possible to deform L_1 into L_2 without crossing H_F . A typical example with $r_v = 3$ is shown in figure 21. However, as we will prove below, there are always one-cycles L'_1, L'_2 in Q which can be continuously deformed into each other without crossing H_F and also satisfy

$$\mathrm{tr}(L_1) - \mathrm{tr}(L_2) = \mathrm{tr}(L'_1) - \mathrm{tr}(L'_2) - (r_v - 1) \mathrm{tr}(vIJ). \quad (3.24)$$

Once such L'_1, L'_2 exist, we can show

$$r_v(JvI) = \mathrm{tr}(L'_1) - \mathrm{tr}(L'_2). \quad (3.25)$$

Since L'_1 can be continuously deformed into L'_2 without crossing H_F , the same argument as in the case of $r_v = 1$ implies that (3.25) vanishes. Since $r_v > 0$, we then find $JvI = 0$.

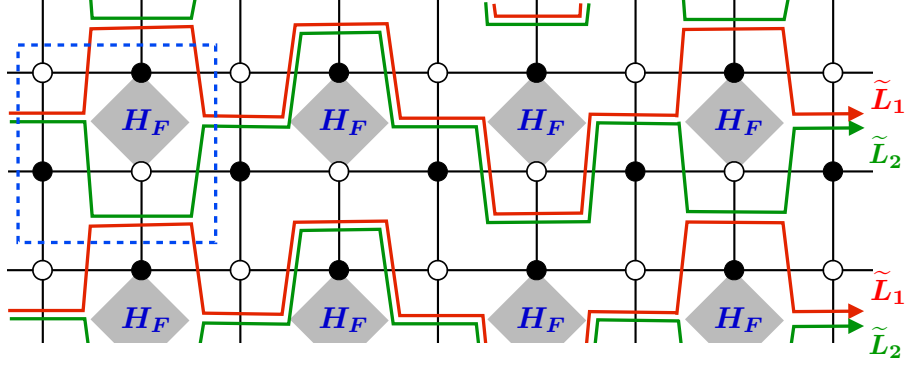


Figure 21: When $r \geq 2$, it is not possible to deform L_1 into L_2 without crossing H_F . The picture shows the universal cover in the case of $r = 3$. The blue dashed rectangle expresses the fundamental domain for the torus $\mathbb{R}^2/\mathbb{Z}^2$.

The remaining task is to show the existence of such a nice set (L'_1, L'_2) . Let us first consider an example in figure 21, where L_1, L_2 are lifted to \tilde{L}_1, \tilde{L}_2 , respectively. We now define paths \tilde{L}'_1 and \tilde{L}'_2 as in figure 22. Since they are periodic in the universal cover, we can regard them as the uplift of some one-cycles of T^2 . We denote such one-cycles by L'_1 and L'_2 , respectively. By definition, L'_1 and L'_2 can be continuously deformed into each other without crossing H_F . Let us now consider the difference between L_1 and L'_1 . In fact, the only difference between them is that, only once, they pass the opposite side of H_F . In terms of u_1, u_2 defined in (3.21), this can be expressed as

$$\text{tr}(L_1) - \text{tr}(L'_1) = \text{tr}(v'u_2) - \text{tr}(v'u_1), \quad (3.26)$$

for some path v' from i to j (figure 23). The relation (3.21) and the F-term equivalence (3.3) now imply that this can be rewritten as

$$\text{tr}(L_1) - \text{tr}(L'_1) = -\text{tr}(v'IJ). \quad (3.27)$$

Note here that v' and v are different paths, but $v'IJ$ and vIJ have the same winding number $r_v(\hat{n}_x, \hat{n}_y)$. In fact, the only difference between v and v' is again that they pass the opposite side of H_F once. Then, the same argument as above implies that there are paths v_1, v_2 (figure 23) from i to j such that

$$\text{tr}(v'IJ) - \text{tr}(vIJ) = \text{tr}(v_1 IJ v_2 IJ). \quad (3.28)$$

Here the right hand side can be written as $(Jv_1 I)(Jv_2 I)$. Note that, since v_1 and v_2 are shorter than v , we always have $r_{v_1}, r_{v_2} < r_v$. Then, due to our assumption, both

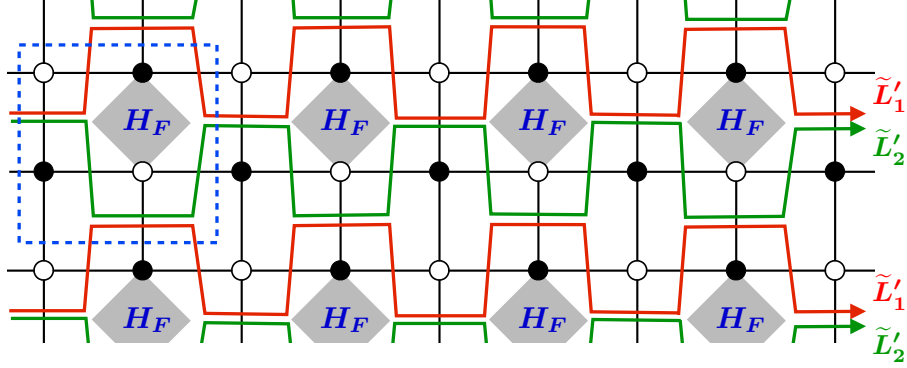


Figure 22: There are always L'_1 and L'_2 which can be deformed into each other without crossing H_F and also satisfy (3.24). The picture shows the uplifts of (L'_1, L'_2) for (L_1, L_2) in figure 21. The blue dashed rectangle expresses the fundamental domain for the torus.

Jv_1I and Jv_2I vanish. This implies that we can rewrite (3.27) as

$$\mathrm{tr}(L_1) - \mathrm{tr}(L'_1) = -\mathrm{tr}(vIJ). \quad (3.29)$$

The minus sign in the right-hand side is important, which comes from the fact that L'_1 always surrounds the *black-node side* of H_F . Let us now turn to L_2 and L'_2 . The similar argument as above tells us that we always have

$$\mathrm{tr}(L_2) - \mathrm{tr}(L'_2) = +\mathrm{tr}(vIJ). \quad (3.30)$$

The different sign in front of $\mathrm{tr}(vIJ)$ is due to the fact that L'_2 always surrounds the *white-node side* of H_F . Combining (3.29) and (3.30), we obtain

$$\mathrm{tr}(L_1) - \mathrm{tr}(L_2) = \mathrm{tr}(L'_1) - \mathrm{tr}(L'_2) - 2\mathrm{tr}(vIJ). \quad (3.31)$$

This is a special example of (3.24) with $r_v = 3$.

By generalizing the above argument, we can show that the existence of the desired (L'_1, L'_2) for any shortest path v which lies inside \mathfrak{R} with $r_v \geq 2$. The crucial point is that the winding number (n_x, n_y) of L_1, L_2 for such v always lies in the convex cone $\mathcal{C}_{\mathcal{D}}$. In general, we can deform L_1, L_2 into the following forms by the F-term equivalence without crossing H_F :

$$L_1 \sim v_{(1)}u_{s_1} \cdots v_{(r_v-1)}u_{s_{r_v-1}}v_{(r_v)}u_1, \quad L_2 \sim v_{(1)}u_{s_1} \cdots v_{(r_v-1)}u_{s_{r_v-1}}v_{(r_v)}u_2, \quad (3.32)$$

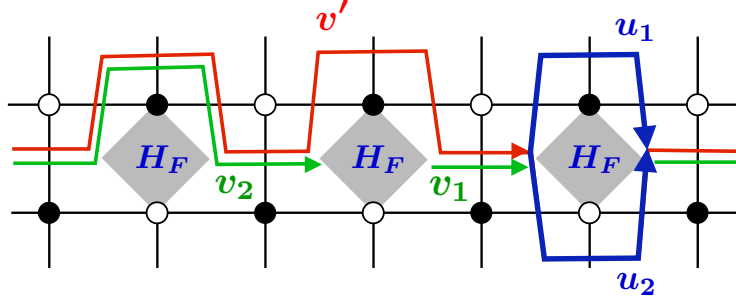


Figure 23: In the example of figure 21, there is a path v' from i to j such that $\text{tr}(L_1) = \text{tr}(v'u_2)$ and $\text{tr}(L'_1) = \text{tr}(v'u_1)$. In the picture, the red path is v' while the blue paths are u_1 and u_2 . The green v_1 and v_2 are used in (3.28).

where $v_{(k)}$ is a shortest path with $r_{v_{(k)}} = 1$, and $s_k \in \{1, 2\}$. Then our desired L'_1, L'_2 are defined by

$$L'_1 = v_{(1)}u_1 \cdots v_{(r_v-1)}u_1v_{(r_v)}u_1, \quad L'_2 = v_{(1)}u_2 \cdots v_{(r_v-1)}u_2v_{(r_v)}u_2. \quad (3.33)$$

The fact that (n_x, n_y) lies in the convex cone $\mathcal{C}_{\mathcal{D}}$ guarantees that L'_1 can be deformed into L'_2 without crossing H_F . The difference between $\text{tr}(L_1)$ and $\text{tr}(L'_1)$ is generally expressed as

$$\text{tr}(L_1) - \text{tr}(L'_1) = -n_1\text{tr}(vIJ), \quad (3.34)$$

where $n_1 = \sum_{k=1}^{r_v-1} (s_k - 1) \geq 0$. Here, we used our assumption that $Jv'I = 0$ for any shortest path v' with $r_{v'} < r_v$. Similarly, the difference between $\text{tr}(L_2)$ and $\text{tr}(L'_2)$ is written as

$$\text{tr}(L_2) - \text{tr}(L'_2) = +n_2\text{tr}(vIJ), \quad (3.35)$$

where $n_2 = \sum_{k=1}^{r_v-1} (2 - s_k) \geq 0$. Then we obtain

$$\text{tr}(L_1) - \text{tr}(L_2) = \text{tr}(L'_1) - \text{tr}(L'_2) - (r_v - 1)\text{tr}(vIJ), \quad (3.36)$$

where we used the fact that $n_1 + n_2 = r_v - 1$. Thus, we have shown the existence of the desired (L'_1, L'_2) , which completes our proof of $J = 0$.

3.8 Proof of $m_{\mathcal{D}} = 0$

We here prove (3.6) on a θ -stable module with $\theta_k < 0$ for $k \in Q_1$. Since such a θ -stable module is a cyclic module generated by an element $\mathbf{m} \in M_*$, it is sufficient to show

that if $Y \in \tilde{Q}_1$ satisfies $(\psi \circ p)(Y) \in m_{\mathcal{D}}$ then $YvI = 0$ for any path v from $\tilde{i} \in \tilde{Q}_0$.²² According to the argument in the previous subsection, we here set $J = 0$.

Let $s(Y)$ be the starting node of Y . We assume v is a path from \tilde{i} to $s(Y)$ because otherwise $YvI = 0$ trivially holds. Moreover, it is sufficient to consider only the shortest path $v = v_{s(Y)}$ from \tilde{i} to $s(Y)$. To see this, recall that v has the standard form (3.18) for the shortest path $v_0 = v_{s(Y)}$ and a loop ω starting with X_F . As shown in [4], this can also be expressed as

$$v = \tilde{\omega}^\ell v_{s(Y)}, \quad (3.37)$$

where $\tilde{\omega}$ is a loop which starts at $s(Y)$ and surrounds a face in \tilde{Q}_2 . In particular, we can take $\tilde{\omega}$ to start with Y . Then $YvI = 0$ immediately follows if $Yv_{s(Y)}I = 0$. Hence, we only need to consider the case $v = v_{s(Y)}$ in our proof.

The remaining task is to prove $Yv_{s(Y)}I = 0$ for $Y \in \tilde{Q}_1$ satisfying $(\psi \circ p)(Y) \in m_{\mathcal{D}}$. Let us first consider $Y \in \tilde{Q}_1$ which is an out-going arrow from \mathfrak{R} . Recall that such Y is always an element of $\text{Zig}(\tilde{\mathcal{P}}_1) \cup \text{Zag}(\tilde{\mathcal{P}}_2)$, and therefore satisfies $(\psi \circ p)(Y) \in m_{\mathcal{D}}$. The path $Yv_{s(Y)}I$ for such Y has already been considered in the previous subsection, and shown to vanish. This also implies that *any* $Y \in \tilde{Q}_1$ outside \mathfrak{R} leads to $Yv_{s(Y)}I = 0$.

Now, let us consider $Y \in \tilde{Q}_1$ which is inside \mathfrak{R} and satisfies $(\psi \circ p)(Y) \in m_{\mathcal{D}}$. We here denote by $t(Y)$ the ending node of Y . Since $t(Y)$ is inside \mathfrak{R} , our lemma in subsection 3.7 implies that the shortest path $v_{t(Y)}$ does not cross $(p^\vee)^{-1}(m_{\mathcal{D}})$. Now, let $\omega_{t(Y)}$ be a loop around a face in \tilde{Q} which starts at $t(Y)$ and ends with Y . We then define a path u_Y so that $\omega_{t(Y)} = Y u_Y$ (figure 24). Here, the path $u_Y v_{t(Y)}$ is a path from \tilde{i} to $s(Y)$ without crossing $(p^\vee)^{-1}(m_{\mathcal{D}})$, which implies that $u_Y v_{t(Y)}$ is a shortest path to $s(Y)$. We can then write $v_{s(Y)} = u_Y v_{t(Y)}$ up to the F-term equivalence, and therefore

$$Yv_{s(Y)}I = Y u_Y v_{t(Y)}I = \omega_{t(Y)} v_{t(Y)}I. \quad (3.38)$$

As mentioned already, $\omega_{t(Y)} v_{t(Y)}$ is F-term equivalent to $v_{t(Y)}\omega$ where ω is a loop starting with X_F . Since $v_{t(Y)}\omega I$ starts with $X_F I$, it vanishes due to the constraint (3.2). Thus we find $Yv_{s(Y)}I = 0$. Combining the argument in the previous paragraph, we have shown $Yv_{s(Y)}I = 0$ for Y which is inside \mathfrak{R} and satisfies $(\psi \circ p)(Y) \in m_{\mathcal{D}}$. This completes our proof.

²²Recall here that $\psi : Q \rightarrow Q^\vee$ is the dual map.

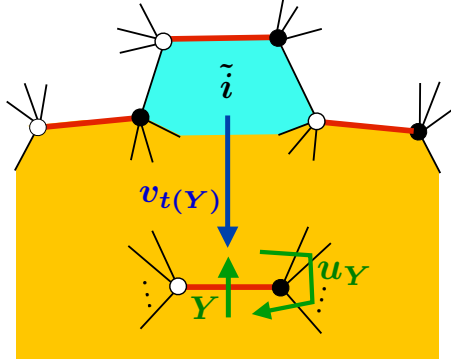


Figure 24: There is always a path from \tilde{i} to $t(Y)$ without crossing $(p^\vee)^{-1}(m_{\mathcal{D}})$ if Y is inside \mathfrak{A} . Then $u_Y v_{t(Y)}$ is a shortest path from \tilde{i} to $s(Y)$. Here the red edges are the ones in $(p^\vee)^{-1}(m_{\mathcal{D}})$.

4 Examples

In this section, we consider some examples of our crystal melting model for D4-D2-D0 states on toric Calabi-Yau three-folds.

4.1 \mathbb{C}^3

The first example is \mathbb{C}^3 , where we can put a single D6-brane on the whole \mathbb{C}^3 or a D4-brane on a divisor \mathbb{C}^2 . In either case, we have no D2-brane charge because \mathbb{C}^3 has no compact two-cycle.

Let us first consider the D6-D0 bound states. The toric diagram and the brane tiling of \mathbb{C}^3 are shown in figure 25. In the quiver quantum mechanics on the D0-branes, we have one gauge group and three chiral multiplets B_a . The rank of the gauge group is equal to the D0-charge. The quiver diagram of the theory is shown in the right picture of figure 25. From the brane tiling, the superpotential is read off as

$$W_0 = \text{tr}(B_1[B_2, B_3]) \quad (4.1)$$

which implies the F-term condition

$$[B_a, B_b] = 0. \quad (4.2)$$

This implies that any element of Δ_* is now expressed as a monomial of the form $(B_1)^{n_1}(B_2)^{n_2}(B_3)^{n_3}I$ for $n_i \in \mathbb{N}$. The periodic dimer model \tilde{Q}^\vee is depicted as in

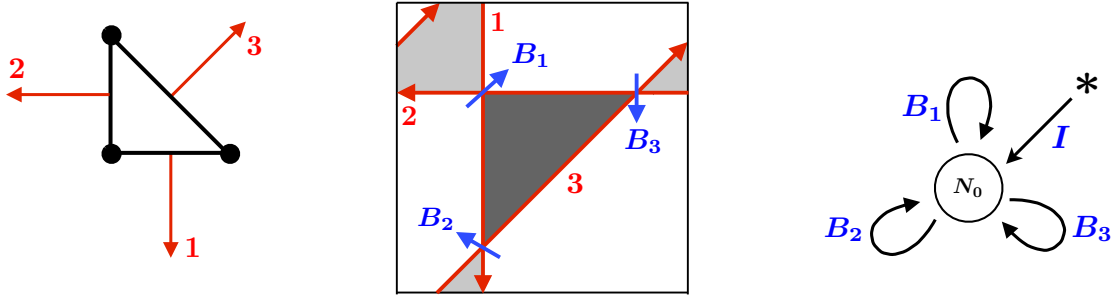


Figure 25: Left: The toric diagram of \mathbb{C}^3 . The lattice points are at $(0, 0)$, $(1, 0)$ and $(0, 1)$. Middle: The brane tiling for D0-branes on \mathbb{C}^3 . Right: The quiver diagram for D6-D0 states on \mathbb{C}^3 .

the left picture of figure 26. Note that this dimer model clearly admits an isoradial embedding.²³ By putting atoms on the faces of \tilde{Q}^\vee , we obtain a cubic crystal as in the right picture of figure 26, where a single cube is an atom associated with the unit D0-charge. Each face of the cube expresses a “bond” associated with a chiral multiplet B_a . The melting rule of the crystal implies that the partition function (2.9) is now written as a sum over three-dimensional Young diagrams \mathfrak{p} [2, 11]:

$$\mathcal{Z}_{\text{D6-D0}} = \sum_{\mathfrak{p}} q^{|\mathfrak{p}|} = \prod_{n=1}^{\infty} \frac{1}{(1 - q^n)^n}. \quad (4.3)$$

where q is the Boltzmann weight for D0-charge.

Now, instead of the D6-brane, let us put a D4-brane on a holomorphic divisor \mathbb{C}^2 in \mathbb{C}^3 . We consider BPS D0-branes bound to the D4-brane. Recall that this example has already been mentioned in the introduction. The perfect matchings of Q^\vee are shown in figure 27. We have three perfect matchings, corresponding to the three corners of the toric diagram of \mathbb{C}^3 . Let us assume, without loss of generality, that the divisor \mathcal{D} wrapped by the D4-brane is associated with the lattice point $(0, 1)$ of the diagram. Then, the boundary NS5-branes of the facet \mathfrak{F} are the second and third NS5-branes in figure 25. Since B_3 is located at their intersection, we identify $X_F = B_3$ in this case. The superpotential induced by the D4-brane is then written as

$$W_{\text{flavor}} = JB_3I. \quad (4.4)$$

The perfect matching $m_{\mathcal{D}}$ only involves B_3 , and therefore the condition (3.6) just implies $B_3 = 0$ on supersymmetric vacua. Setting $B_3 = 0$ in fact leads to the well-

²³See appendix B for a general criterion.

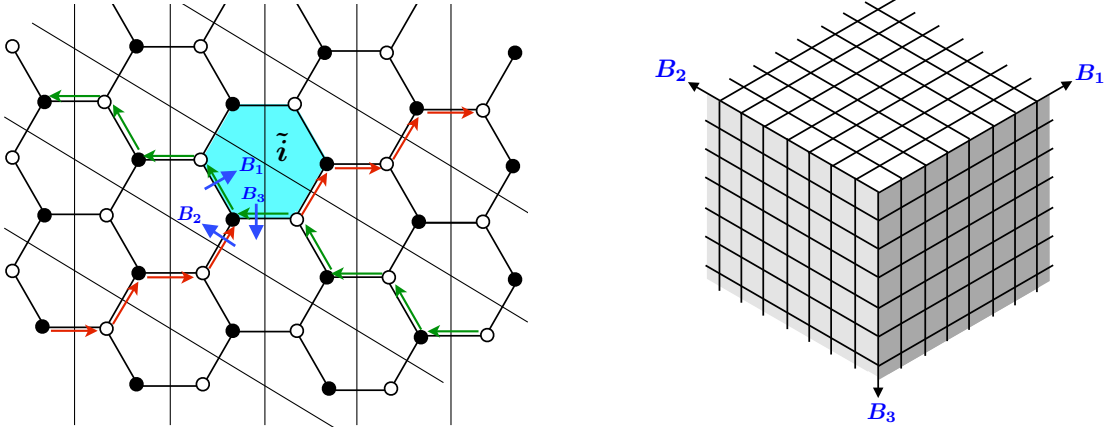


Figure 26: Left: The universal cover \tilde{Q}^\vee of the dimer model Q^\vee for \mathbb{C}^3 . Each diamond region is a fundamental domain of $\mathbb{R}^2/\mathbb{Z}^2 \simeq T^2$. The two zig-zag paths which are attached to \tilde{i} and share B_3 at their intersection are also shown. Right: The corresponding three-dimensional crystal is obtained by putting atoms on the faces of \tilde{Q}^\vee .

known D4-D0 quiver on \mathbb{C}^2 (figure 28). The only non-trivial F-flatness condition is now

$$[B_1, B_2] + IJ = 0, \quad (4.5)$$

which is equivalent to the ADHM constraint. Thus, we have reproduced the well-known result of the D4-D0 states on \mathbb{C}^2 . Note that we already know that $J = 0$ also holds on supersymmetric vacua.

The $U(1)^2$ -fixed points of the moduli space are in one-to-one correspondence with the molten configurations of a two-dimensional crystal in figure 28, where a single square atom is associated with the unit D0-charge. The four sides of each square express four “bonds” attached to it. Note that the crystal is a two-dimensional “slope face” of the three-dimensional crystal in figure 26. Moreover, the boundary of the two-dimensional crystal is given by the two zig-zag paths shown in the left picture of figure 26. The melting rule of the crystal implies that every molten configuration is expressed as a two-dimensional Young diagram. The partition function (3.12) is then written as a sum over two-dimensional Young diagrams \mathbf{p} :

$$\mathcal{Z}_{\text{D4-D0}} = \sum_{\mathbf{p}} q^{|\mathbf{p}|} = \prod_{n=1}^{\infty} \frac{1}{1 - q^n}. \quad (4.6)$$

We here implicitly assume that all the fixed points are bosonic. We can show this by

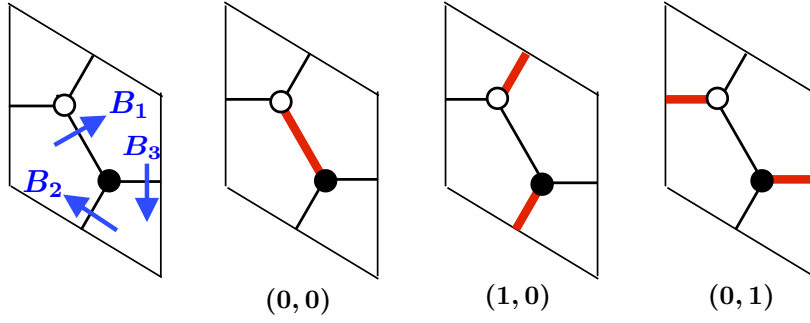


Figure 27: Leftmost: The dimer model Q^\vee on T^2 for \mathbb{C}^3 . Others: Three perfect matchings corresponding to the three lattice points of the toric diagram. In \mathbb{C}^3 case, the perfect matchings are in one-to-one correspondence with the toric divisors of \mathbb{C}^3 .

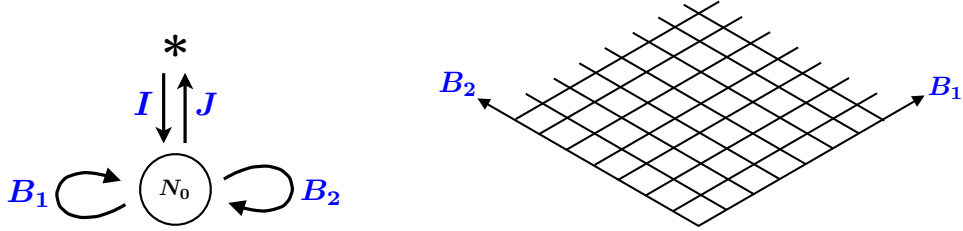


Figure 28: Left: The quiver diagram for D4-D0 states when \mathcal{D} is associated with the lattice point $(0, 1)$ of the toric diagram. Right: The two-dimensional crystal for the D4-D0 states on \mathbb{C}^2 .

calculating the dimension of the moduli space. The moduli space is parameterized by I, J, B_1 and B_2 which have $2|\mathbf{p}| + 2|\mathbf{p}|^2$ complex parameters. They are subject to the F-term conditions $[B_1, B_2] + IJ = 0$ which reduces $|\mathbf{p}|^2$ of them. Furthermore, dividing out the gauge degrees of freedom reduces further $|\mathbf{p}|^2$ complex parameters. Thus, the complex dimension of the moduli space is

$$\dim_{\mathbb{C}}(\mathcal{M}_{|\mathbf{p}|}) = 2|\mathbf{p}|, \quad (4.7)$$

which implies that all the fixed points of the moduli space are bosonic. Note that (4.7) matches the dimension of $|\mathbf{p}|$ -instanton moduli space.

4.2 Conifold

The second example is the conifold. We have already seen the brane tiling, D6-D2-D0 quiver, and D6-D2-D0 crystal in section 2. The partition function associated with

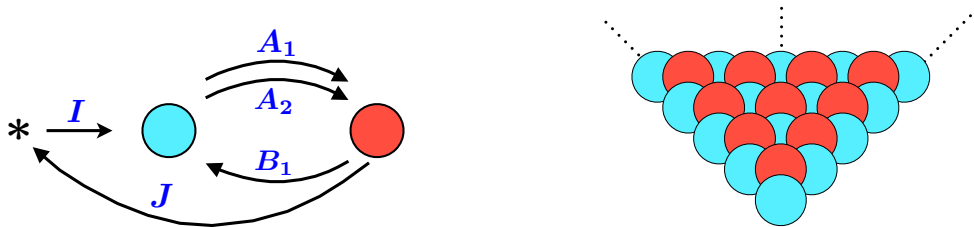


Figure 29: Left: The quiver diagram for D4-D2-D0 states on the conifold. Right: The reduced crystal is a two-dimensional slope face of the three-dimensional pyramid crystal in figure 6.

the three-dimensional melting crystal in figure 6 was considered in [3] in the study of the non-commutative Donaldson-Thomas invariants. In this subsection, we instead consider D4-D2-D0 states on the conifold. Note that the dimer model Q^\vee for the conifold in figure 5 admits an isoradial embedding.

We first put a flavor D4-brane on a toric divisor \mathcal{D} associated with a corner of the toric diagram in figure 2. Since all the toric divisors are isomorphic in the singular conifold limit, we assume without loss of generality that \mathcal{D} is associated with the lattice point $(1, 1)$ of the toric diagram. The boundary NS5-branes are then the first and second ones in the right picture of figure 3. Since B_2 comes from the massless string at their intersection, X_F is identified with B_2 in this case. The superpotential induced by the D4-brane is written as

$$W_{\text{flavor}} = JB_2I. \quad (4.8)$$

The total superpotential is given by $W_0 + W_{\text{flavor}}$ with

$$W_0 = \text{tr}(A_1B_2A_2B_1) - \text{tr}(A_1B_1A_2B_2). \quad (4.9)$$

The perfect matching $m_{\mathcal{D}}$ turns out to be m_3 in figure 9. According to (3.6), placing a D4-brane on \mathcal{D} eliminates all the chiral fields involved in $m_{\mathcal{D}}$ from the massless spectrum, leading to a quiver diagram shown in the left picture of figure 29. The non-trivial F-term condition is now

$$A_2B_1A_1 - A_1B_1A_2 + IJ = 0. \quad (4.10)$$

The two-dimensional crystal for the D4-D2-D0 states then extends in the region \mathfrak{R} in figure 12. As shown in the right picture of figure 29, this crystal is a two-dimensional

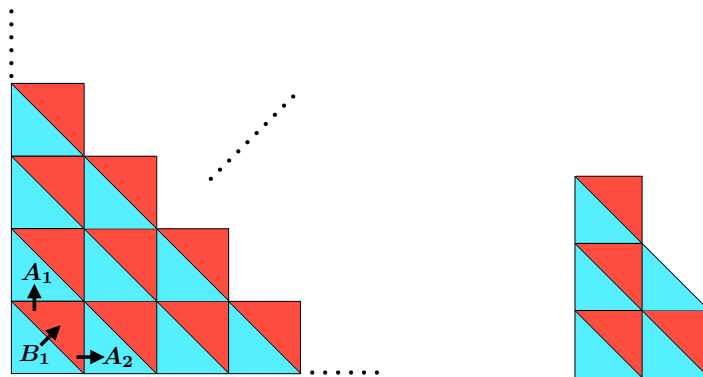


Figure 30: Left: The two-dimensional crystal for D4-D2-D0 states on the conifold, which infinitely extends in the upper-right region. Three chiral fields A_1, A_2, B_2 correspond to three types of “bonds” connecting triangle atoms. Right: An example of a molten crystal.

“slope face” of the three-dimensional pyramid crystal in figure 6. Note here that we already know that $J = 0$ also follows on the supersymmetric vacua.

Let us express the two-dimensional crystal in a different way, keeping the crystalline structure. We express each atom as a triangle so that its three sides are associated with the three “bonds” attached to the atom. Then the two-dimensional crystal in figure 29 is re-expressed as in the left of figure 30. This two-dimensional crystal is precisely equivalent to that of the triangular partition model proposed in [13]. The melting rule of the crystal implies that

- A blue triangle can be removed if and only if its left and lower edges are not attached to other atoms.
- A red triangle can be removed if and only if its slope edge is not attached to other atoms.

These are exactly the same rules as proposed in [13].

The partition function of the BPS index is written as a sum over the molten configurations of the crystal:

$$\mathcal{Z}_{\text{crystal}} := \sum_{\mathfrak{p}} (-1)^{\dim_{\mathbb{C}}(\mathcal{M}_{a,b})} x^a y^b, \quad (4.11)$$

where \mathfrak{p} runs over all the molten configurations, and a and b are the numbers of blue and red triangular atoms in \mathfrak{p} . The sign factor is determined by the dimension of

the moduli space. We now have five non-vanishing chiral fields I, J, A_1, A_2, B_1 with $3ab + a + b$ complex degrees of freedom in total. The non-trivial F-term condition (4.10) reduces ab of them. Dividing out the gauge degrees of freedom further reduces $a^2 + b^2$ parameters. Thus, the dimension of the moduli space is written as

$$\dim_{\mathbb{C}}(\mathcal{M}_{a,b}) = a + b - (a - b)^2. \quad (4.12)$$

This implies that

$$(-1)^{\dim_{\mathbb{C}}(\mathcal{M}_{a,b})} = 1, \quad (4.13)$$

and therefore the fixed points of the moduli space are all bosonic.²⁴ When we change the variables as

$$q = xy, \quad Q = -x, \quad (4.14)$$

the partition function (4.11) can be rewritten as [13]

$$\mathcal{Z}_{\text{crystal}} = \prod_{n=1}^{\infty} \frac{1}{1 - q^n} \prod_{m=0}^{\infty} (1 - q^m Q). \quad (4.15)$$

By identifying q and Q with the Boltzmann weights for D0 and D2-branes respectively, this corresponds to the correct BPS D4-D2-D0 partition function in the singular limit of the conifold [58].

4.3 Suspended pinch point

The third example is the suspended pinch point, whose toric diagram is shown in the left picture of figure 31. In this case, we have four toric divisors associated with the corners of the toric diagram. We first consider a D4-brane on the divisor for p_1 , and next consider that for p_2 . The former reproduces the *oblique partition model* proposed in [14] while the latter gives a new statistical model. It will be shown via the wall-crossing formula that they give the correct partition function of the BPS indices for the corresponding D4-D2-D0 states.

D2-D0 Quiver and bipartite graph

We first identify the quiver diagram for the D2-D0 states on the suspended pinch point. The relevant brane tiling is shown in the middle of figure 31. The quiver diagram of the

²⁴Note here (4.12) is always non-negative. In fact, our melting crystal implies $b \geq \frac{(a-b)(a-b-1)}{2}$, which is equivalent to $a + b \geq (a - b)^2$.

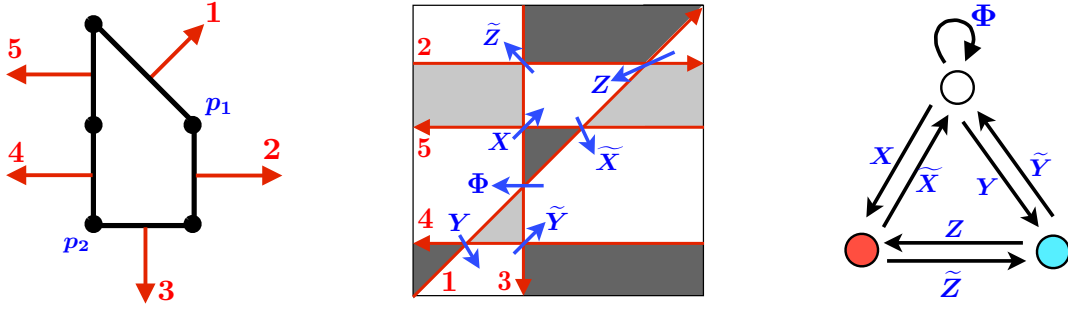


Figure 31: Left: The toric diagram of the suspended pinch point. Right: The brane tiling for the D2-D0 states on the suspended pinch point singularity.

theory on the D-branes is shown in the right picture. We have seven chiral multiplets with the following superpotential:

$$W_0 = \text{tr} \left(\Phi(\tilde{Y}Y - \tilde{X}X) \right) + \text{tr} \left(Z\tilde{Z}X\tilde{X} \right) - \text{tr} \left(\tilde{Z}ZY\tilde{Y} \right). \quad (4.16)$$

The F-term conditions are then written as

$$\begin{aligned} \tilde{Y}Y &= \tilde{X}X, & \tilde{Z}X\tilde{X} &= Y\tilde{Y}\tilde{Z}, & X\tilde{X}Z &= ZY\tilde{Y}, \\ \Phi\tilde{X} &= \tilde{X}Z\tilde{Z}, & X\Phi &= Z\tilde{Z}X, & \Phi\tilde{Y} &= \tilde{Y}\tilde{Z}Z, & Y\Phi &= \tilde{Z}ZY. \end{aligned} \quad (4.17)$$

If we introduce a flavor D6-brane, then we have a D6-node attached to one of the nodes in the quiver diagram without any additional superpotential. The $U(1)^3$ -fixed points of the moduli space are expressed as molten configurations of the three-dimensional crystal studied in [5] (In particular, see figure 5).

In this subsection, we instead introduce a flavor D4-brane on a toric divisor. The dimer model Q^\vee and its perfect matchings are shown in figure 32. Note that Q^\vee admits an isoradial embedding.

Oblique partition model

We first put a D4-brane on a divisor associated with the lattice point p_1 of the toric diagram. The boundary NS5-branes for the divisor are the first and the second NS5-branes in figure 31. Since the chiral multiplet Z comes from the massless string at the intersection of the boundary NS5-branes, it is Z that should be identified with X_F in this case. This implies that our D4-node $*$ is now attached to the blue and red nodes in the quiver diagram. The additional superpotential induced by the D4-brane is now

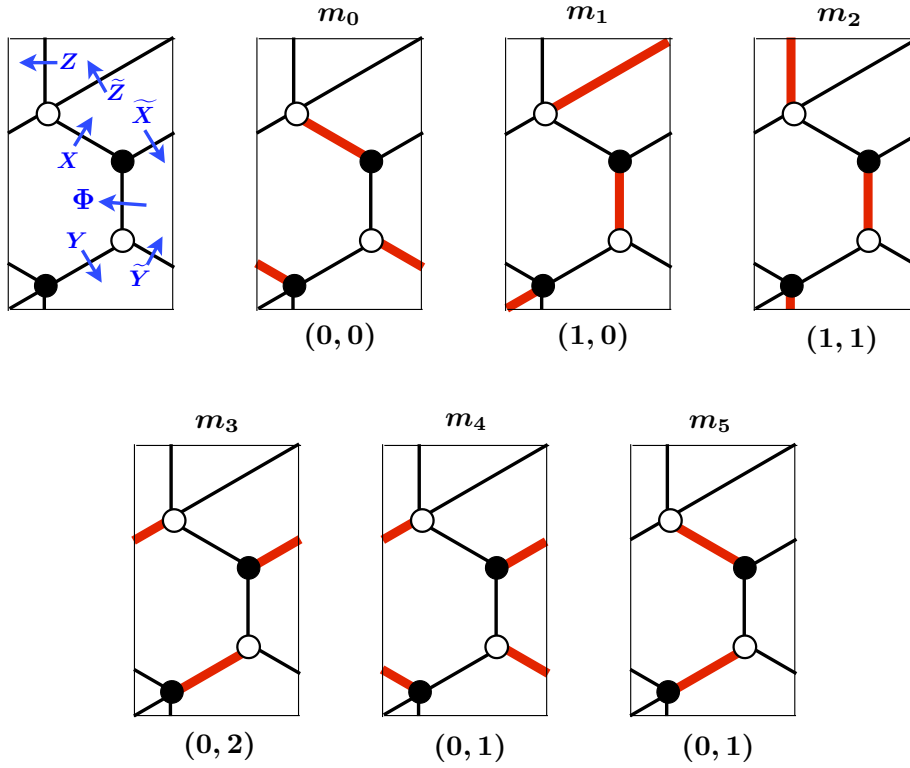


Figure 32: The dimer model Q^\vee and perfect matchings for the suspended pinch point singularity. The coordinate below each perfect matching expresses the corresponding lattice point of the toric diagram.

written as

$$W_{\text{flavor}} = JZI. \quad (4.18)$$

As shown in figure 32, the perfect matching associated with p_1 is m_2 , which includes Z and Φ . The constraint (3.6) on supersymmetric vacua is now written as

$$Z = 0, \quad \Phi = 0. \quad (4.19)$$

This means that Z and Φ become massive with vanishing vev's in the infrared. The quiver diagram from which the two massive fields are eliminated is shown in the left picture of figure 33. The non-trivial F-term conditions are now

$$\tilde{Y}Y - \tilde{X}X = 0, \quad \tilde{Z}X\tilde{X} - Y\tilde{Y}\tilde{Z} + IJ = 0. \quad (4.20)$$

Note here that, from the general argument in the previous section, we already know that $J = 0$ also follows on the supersymmetric vacua. We here explicitly write J for comparison with the previous \mathbb{C}^3 example.

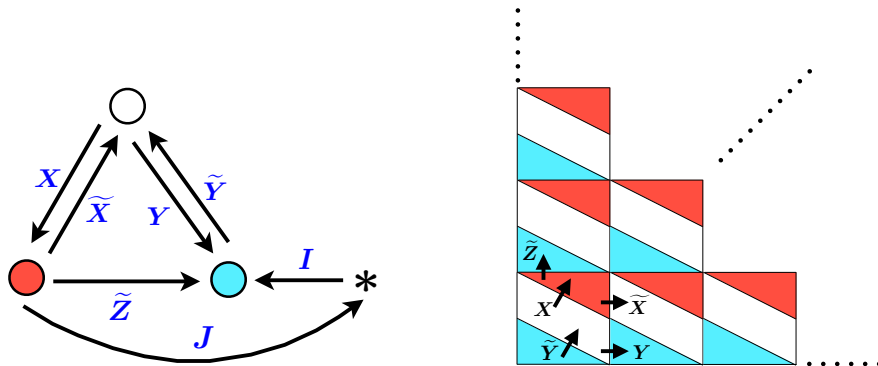


Figure 33: Left: The quiver diagram for the D4-D2-D0 states when the D4-brane is on a divisor associated with p_1 in the toric diagram. The D4-node is denoted by $*$. Right: The two-dimensional crystal for the D4-D2-D0 states, which reproduces the so-called “oblique partition model” proposed in [14].

The two-dimensional crystal for the D4-D2-D0 states is expressed as in the right picture of figure 33, where each atom is assigned the same color as the corresponding quiver node. The (three or four) sides of each atom are associated with “bonds” attached to it. This crystal is the same as that in the “oblique partition model” proposed in [14]. Our melting rule of the crystal implies the followings:

- A blue triangle can be removed if and only if its left and lower edges are not attached to other atoms.
- A red triangle can be removed if and only if its slope edge is not attached to other atoms.
- A parallelogram can be removed if and only if its left and lower edges are not attached to other atoms.

These are exactly the same rules as proposed in [14]. Note that, as mentioned in the previous section, this two-dimensional crystal is a “slope face” of the three-dimensional crystal associated with the parent D6-D2-D0 states.

The partition function of the BPS index is evaluated by counting molten configurations \mathbf{p} of the two-dimensional crystal:

$$\mathcal{Z}_{\text{crystal}} = \sum_{\mathbf{p}} (-1)^{\dim_{\mathbb{C}}(\mathcal{M}_{a,b,c})} x^a y^b z^c, \quad (4.21)$$

where a, b, c are the numbers of blue triangles, red triangles and white parallelograms in \mathfrak{p} , respectively. The variables x, y, z are the Boltzmann weights for the atoms. The sign factor is determined by the dimension of the moduli space $\mathcal{M}_{a,b}$. We now have seven non-vanishing chiral fields with $(a+b+ab+2bc+2ca)$ complex degrees of freedom in total. The non-trivial F-term conditions (4.20) reduce (c^2+ab) of them. The gauge degrees of freedom reduce further $(a^2+b^2+c^2)$ parameters. Thus the dimension of the moduli space is given by

$$\dim_{\mathbb{C}}(\mathcal{M}_{a,b,c}) = a + b + 2bc + 2ca - 2c^2 - a^2 - b^2. \quad (4.22)$$

Then the sign factor is given by

$$(-1)^{\dim_{\mathbb{C}}(\mathcal{M}_{a,b,c})} = 1. \quad (4.23)$$

In terms of different variables

$$q = xyz, \quad Q_1 = -x, \quad Q_2 = z, \quad (4.24)$$

the partition function is written as

$$\mathcal{Z}_{\text{crystal}} = \prod_{n=1}^{\infty} \frac{1}{1-q^n} \prod_{m=0}^{\infty} (1-q^m Q_1)(1-q^m Q_1 Q_2). \quad (4.25)$$

It was shown in [14] via wall-crossing formula that this is the correct BPS partition function of the D4-D2-D0 states on the suspended pinch point singularity, where q is the Boltzmann weight for D0-charge and Q_1, Q_2 are those for D2-charges associated with two blowup two-cycles.

Another statistical model

We now put a D4-brane on the divisor associated with p_2 in figure 31. The boundary NS5-branes are then the third and fourth ones in figure 31. Since \tilde{Y} comes from the string at the intersection of the boundary NS5-branes, X_F is now identified with \tilde{Y} . This implies that the D4-node $*$ is attached to the blue and white nodes in the quiver diagram. The superpotential induced by the D4-brane is now written as

$$W_{\text{flavor}} = J\tilde{Y}I. \quad (4.26)$$

The perfect matching associated with the lattice point p_2 is m_0 in figure 32. The constraint (3.6) then implies that

$$X = 0, \quad \tilde{Y} = 0, \quad (4.27)$$

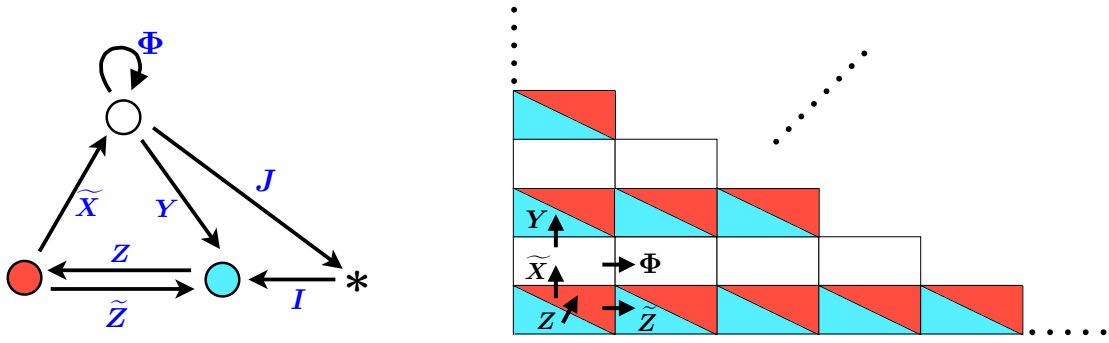


Figure 34: Left: The quiver diagram of the theory on D4-D2-D0 states with a D4-brane on a divisor associated with p_2 in the toric diagram. Right: The corresponding two-dimensional crystal.

in the infrared. After eliminating X and \tilde{Y} , the quiver diagram can be depicted as in the left picture of figure 34. The non-trivial F-term conditions are now

$$\Phi\tilde{X} - \tilde{X}Z\tilde{Z} = 0, \quad Y\Phi - \tilde{Z}ZY + IJ = 0. \quad (4.28)$$

Although $J = 0$ also follows in the infrared, we here explicitly write it for comparison with the other examples.

The two-dimensional crystal can be depicted as in the right picture of figure 34. Note that this crystal is an *another* “slope face” of the *same* three-dimensional crystal for the parent D6-D2-D0 states. In fact, choosing a different divisor \mathcal{D} of the same Calabi-Yau leads to a different slope face of the same three-dimensional crystal. The melting rule of the crystal now implies

- A blue triangle can be removed if and only if its left and lower edges are not attached to other atoms.
- A red triangle can be removed if and only if its slope edge is not attached to other atoms.
- A white rectangle can be removed if and only if its left and lower edges are not attached to other atoms.

This two-dimensional melting crystal model is, to the best of our knowledge, a new example of statistical model for D4-D2-D0 states. We therefore examine it in detail. The partition function of the BPS index of the D4-D2-D0 states is given by

$$\mathcal{Z}_{\text{crystal}} = \sum_{\mathfrak{p}} (-1)^{\dim_{\mathbb{C}}(\mathcal{M}'_{a,b,c})} x^a y^b z^c, \quad (4.29)$$

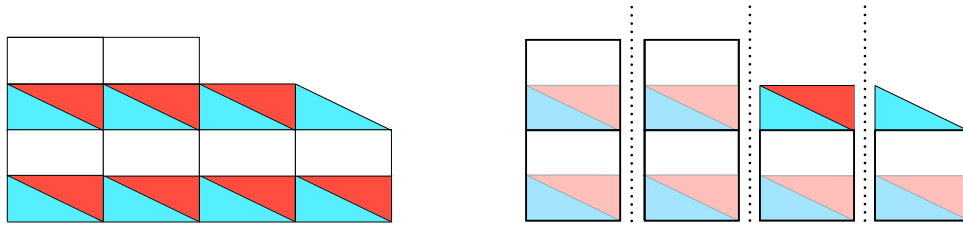


Figure 35: Left: A molten configuration of the crystal. Right: The left configuration is split into towers of atoms. Each tower has several squares composed of a blue triangle, a red triangle and a white rectangle. Some of the towers have an additional blue triangle with or without a red triangle on its top.

where a, b, c are the numbers of blue triangles, red triangles and white rectangles in \mathfrak{p} , respectively. The variables x, y and z are Boltzmann weights for the three types of atom. The sign factor is determined by the dimension of the moduli space $\mathcal{M}'_{a,b,c}$. We here have seven massless chiral fields with $(a + c + 2ab + bc + ca + c^2)$ complex degrees of freedom in total. The F-term conditions (4.28) reduce $(bc + ca)$ of them. The gauge degrees of freedom reduce further $(a^2 + b^2 + c^2)$ parameters. Then the dimension of the moduli space is

$$\dim_{\mathbb{C}}(\mathcal{M}'_{a,b,c}) = a + c + 2ab - a^2 - b^2, \quad (4.30)$$

which implies

$$(-1)^{\dim_{\mathbb{C}}(\mathcal{M}'_{a,b,c})} = (-1)^{b+c}. \quad (4.31)$$

What is interesting here is that, by changing the variables as

$$q = xyz, \quad Q_1 = -x, \quad \tilde{Q}_2 = y, \quad (4.32)$$

we can write (4.29) as

$$\mathcal{Z}_{\text{crystal}} = \prod_{n=1}^{\infty} \frac{1}{1 - q^n} \prod_{m=0}^{\infty} \frac{1 - q^m Q_1}{1 - q^m Q_1 \tilde{Q}_2}. \quad (4.33)$$

To see this, let us consider a molten configuration of the crystal as in the left picture of figure 35, and split it into towers of atoms as in the right picture. Each such tower includes several squares composed of a blue triangle, a red triangle and a white rectangle. The relation (4.32) implies that each such square contributes q to the partition function. Furthermore, some of the towers have an additional blue triangle

with or without an additional red triangle on their top. According to (4.32), an additional blue (or red) triangle contribute $-Q_1$ (or $-\tilde{Q}_2$) to the partition function. Thus, in general, we have the following three types of tower:

1. A tower which has $k(> 0)$ squares without any additional triangles on its top. This contributes q^k to the partition function.
2. A tower which has $k(\geq 0)$ squares with an additional blue triangle on its top. This contributes $-q^k Q_1$ to the partition function.
3. A tower which has $k(\geq 0)$ squares with an additional blue and a red triangle on its top. This contributes $q^k Q_1 \tilde{Q}_2$ to the partition function.

The whole contribution from a molten configuration \mathbf{p} is the multiplication of contributions from all the towers in \mathbf{p} . For example, \mathbf{p} in figure 35 contributes $q^6 Q_1^2 \tilde{Q}_2$. Note here that any molten configuration \mathbf{p} is a collection of some towers, but the converse is not true. Namely, not all collections of towers give a molten configuration of the crystal. In particular, for fixed k , a single molten configuration \mathbf{p} can include at most one second type of tower, while the first and the third types have no such restriction. This follows from our melting rule of the crystal. Thus, the first and the third types are “bosonic” while the second type is “fermionic.” Summing up all the molten configurations is now equivalent to considering all the collections of the “bosonic” and “fermionic” towers. The bosonic towers contribute

$$\prod_{n=1}^{\infty} \frac{1}{1 - q^n} \prod_{m=0}^{\infty} \frac{1}{1 - q^m Q_1 \tilde{Q}_2} \quad (4.34)$$

to the partition function, while the fermionic towers contribute

$$\prod_{m=0}^{\infty} (1 - q^m Q_1). \quad (4.35)$$

Then we find that the total partition function is given by (4.33).

Now, let us show that the partition function (4.33) is consistent with the wall-crossing formula for the BPS index. We use the same method as in [58, 59, 60].²⁵ We first blowup the suspended pinch point singularity so that the divisor \mathcal{D} wrapped by the D4-brane is topologically \mathbb{C}^2 . The toric web-diagram after the blowup is shown in figure 36. The blowup parameters are regarded as the Kähler moduli of the geometry.

²⁵See also [61] for a pictorial representation of the wall-crossing phenomena of D4-D2-D0 states.

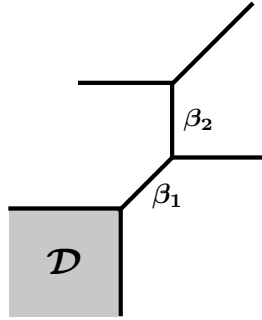


Figure 36: A blowup of the suspended pinch point singularity. We have a D4-brane on \mathcal{D} .

Varying them generically changes the BPS degeneracy of wrapped D-branes, which is called the “wall-crossing phenomenon.” In particular, when we take a large radius limit of the blowup cycle, the BPS partition function becomes very simple [58, 59, 60]. In the large radius limit of the two-cycle β_1 , the geometry near the D4-brane is \mathbb{C}^3 . The two-cycle β_1 now transversally intersects with the divisor \mathcal{D} wrapped by the D4-brane. A perturbative string analysis then tells us that no D2-brane on β_1 can form a BPS bound state with the D4-brane.²⁶ The partition function of the BPS index is then given by the D4-D0 partition function on \mathbb{C}^2 :

$$\mathcal{Z}_0 = \prod_{n=1}^{\infty} \frac{1}{1 - q^n}, \quad (4.36)$$

where q denotes a Boltzmann weight for D0-charge.

We now shrink β_1 and go back to the singular limit of the Calabi-Yau threefold. Between the large radius and singular limits, we have an infinite number of wall-crossing phenomena. Any such wall-crossing is associated with an appearance or disappearance of BPS bound states in the spectrum. Suppose that a BPS bound state with charge Γ decays into two BPS states with charge Γ_1 and Γ_2 .²⁷ The charge and energy conservations imply that such a decay is possible only if

$$\arg Z(\Gamma_1) = \arg Z(\Gamma_2), \quad (4.37)$$

where $Z(\Gamma)$ is the central charge of BPS states with charge Γ . Since the central charge depends on the Kähler moduli, the equation (4.37) can be solved by the moduli

²⁶Note here any α' -correction to the BPS condition is suppressed in the large radius limit.

²⁷Any decay channel involving a non-BPS state does not affect the BPS index.

parameters, which gives us a real codimension one subspace in the moduli space. Such a subspace is called the “wall of marginal stability.” In our case, we are only interested in the charge

$$\Gamma = \mathcal{D} + \sum_{k=1}^2 M_k \beta_k - NdV, \quad (4.38)$$

where β_k is the unit charge for D2-branes on the k -th blowup two-cycle, $-dV$ is the unit D0-charge, and $M_k, N \in \mathbb{Z}$. We take the basis of the two-cycles as in figure 36. We use the same symbol \mathcal{D} in (4.38) to denote the charge for our D4-brane. Since our D4-brane is non-compact, its central charge is divergent. We therefore regularize it to write $Z(\mathcal{D}) = \frac{1}{2}\Lambda^2 e^{2i\varphi}$, where $\Lambda \rightarrow \infty$ should be taken in the final expression. The phase φ expresses the “ratio” of the volume and B-field of the D4-brane and is fixed so that $0 < \varphi < \pi/4$ throughout our discussion. This regularization was first given in [62]. By taking a suitable parameterization of the Kähler moduli space, the central charge of the D2-D0 states can be written as $Z(\beta_k) = z_k$, $Z(-dV) = 1$.²⁸

The possible decay channels relevant for the wall-crossings are then [60]

$$\Gamma_1 = \mathcal{D} + \sum_{k=1}^2 (M_k - m_k) \beta_k - (N - n)dV, \quad \Gamma_2 = \sum_{k=1}^2 m_k \beta_k - ndV, \quad (4.39)$$

which implies

$$Z(\Gamma_1) \sim \frac{1}{2}\Lambda^2 e^{2i\varphi}, \quad Z(\Gamma_2) = \sum_{k=1}^2 m_k z_k + n. \quad (4.40)$$

Here m_k, n express the charges of the D2-D0 fragment. According to the Gopakumar-Vafa invariants [63, 64] for the suspended pinch point,²⁹ the non-vanishing BPS indices of the D2-D0 states turn out to be

$$\Omega(\Gamma_2) = 1 \quad \text{for} \quad (m_1, m_2, n) = (\pm 1, 0, n), (0, \pm 1, n), \quad (4.41)$$

$$\Omega(\Gamma_2) = -1 \quad \text{for} \quad (m_1, m_2, n) = (\pm 1, \pm 1, n). \quad (4.42)$$

Thus, we have walls of marginal stability for $(m_1, m_2, n) = (\pm 1, 0, n)$, $(0, \pm 1, n)$ and $(\pm 1, \pm 1, n)$. The locations of the walls are specified by solving (4.37). In particular, when we fix $z_2 = 1/2$ then the walls are drawn in the complex z_1 -plane as in figure 37, where we denote each wall by $W_n^{m_1, m_2}$. Here $\text{Im } z_2 = 0$ means the two-cycle β_2

²⁸Here $z_k \in \mathbb{C}$ expresses the volume and the B-field of the k -th two-cycle when $\text{Im } z_k$ is large.

²⁹For the explicit calculation of the invariants, see appendix D of [60].

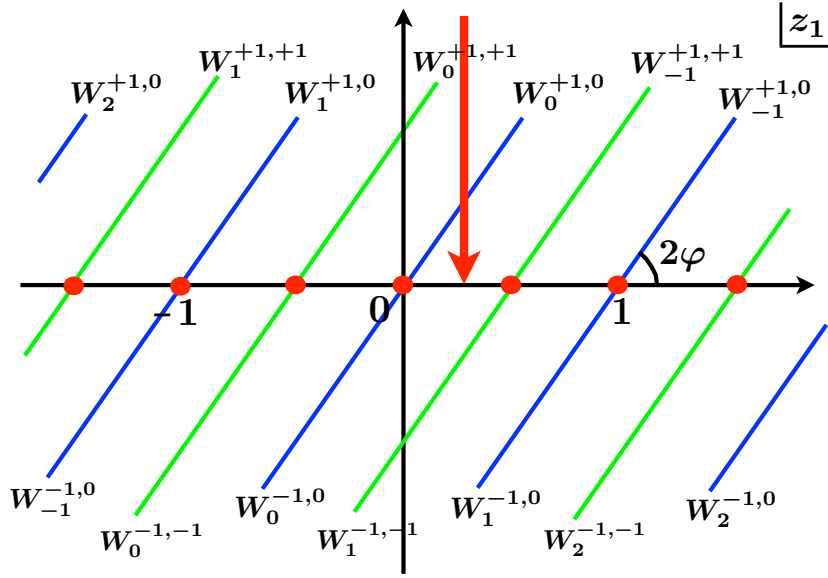


Figure 37: The walls of marginal stability in the complex z_1 -plane with $z_2 = 1/2$. All the walls are semi-infinite line from singular points (red dots). Along the red arrow, we move $\text{Im } z_1$ from ∞ to 0, crossing the walls $W_n^{1,0}$ and $W_n^{1,1}$ for all $n \geq 0$.

shrinks to a point. On the other hand, $\text{Re } z_2 \neq 0$ implies a non-vanishing B-field on β_2 , which is necessary to avoid massless singularities associated with D2-branes wrapping β_2 . Between the large radius and singular limits, we move $\text{Im } z_1$ from $\text{Im } z_1 = +\infty$ to $\text{Im } z_1 = 0$. To avoid massless singularities, we tune $\text{Re } z_1$ so that $0 < \text{Re } z_1 < 1/2$. Then we cross the walls $W_n^{1,0}$ and $W_n^{1,1}$ for all $n \geq 0$ (figure 37).

Since our Γ_1 has no positive integer greater than one which divides out Γ_1 , we can use the so-called “semi-primitive wall-crossing formula” [65]. The formula tells us that the partition function changes at each wall-crossing as

$$\mathcal{Z} \rightarrow \mathcal{Z} \left(1 + (-1)^{\langle \Gamma, \Gamma_2 \rangle} q^n Q_1^{m_1} \tilde{Q}_2^{m_2} \right)^{\langle \Gamma_2, \Gamma \rangle \Omega(\Gamma_2)}, \quad (4.43)$$

where Q_1 and \tilde{Q}_2 are Boltzmann weights for D2-branes on β_1 and β_2 respectively. The bracket $\langle \Gamma, \Gamma_2 \rangle$ is the intersection product of the charges. To be more explicit, it is written as

$$\langle \Gamma, \Gamma_2 \rangle = \sum_{k=1}^2 m_k \langle \mathcal{D}, \beta_k \rangle = m_1, \quad (4.44)$$

where $\langle \mathcal{D}, \beta_k \rangle$ is equivalent to the intersection number of the divisor \mathcal{D} and the blowup cycle β_k . By taking into account all the wall-crossings between the large radius and

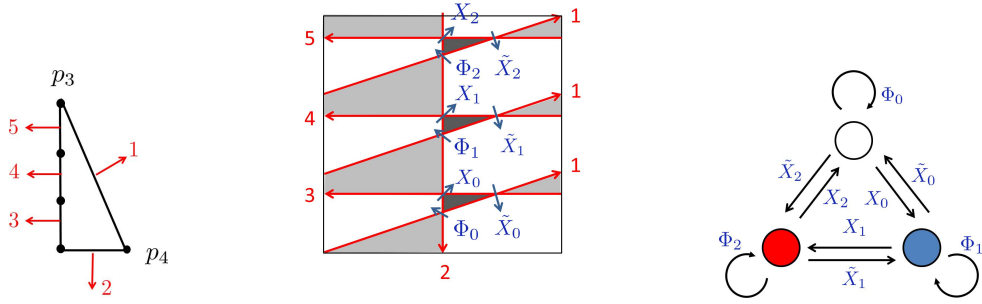


Figure 38: Left: The toric diagram of $\mathbb{C}^2/\mathbb{Z}_3 \times \mathbb{C}$. p_3 and p_4 represent the lattice point $(0, 3)$ and $(1, 0)$ for respectively. Middle: The brane tiling. Right: The quiver diagram for D2-D0 states.

singular limits, we find that the partition function at the singular limit is written as

$$\mathcal{Z}_{\text{D4-D2-D0}} = \mathcal{Z}_0 \prod_{n=0}^{\infty} \frac{1 - q^n Q_1}{1 - q^n Q_1 \tilde{Q}_2} = \prod_{n=1}^{\infty} \frac{1}{1 - q^n} \prod_{m=0}^{\infty} \frac{1 - q^m Q_1}{1 - q^m Q_1 \tilde{Q}_2}, \quad (4.45)$$

which agrees with (4.33).

4.4 Orbifold $\mathbb{C}^2/\mathbb{Z}_N \times \mathbb{C}$

In this subsection, we study two dimensional statistical models for D4-D2-D0 states on $\mathbb{C}^2/\mathbb{Z}_N \times \mathbb{C}$, where the D4-brane wrapping on a non-compact divisor. The toric diagram of $\mathbb{C}^2/\mathbb{Z}_N \times \mathbb{C}$ is represented by the lattice points $(0, 0)$, $(1, 0)$ and $(0, N)$ in \mathbb{Z}^2 . We listed the toric diagram, brane tiling and quiver diagram associated with $\mathbb{C}^2/\mathbb{Z}_3 \times \mathbb{C}$ in the figure 38.

Orbifold partition

The first example is the D4-brane wrapping on the $\mathbb{C}^2/\mathbb{Z}_N$ associated with the lattice point $(1, 0)$. The blow up geometry of $\mathbb{C}^2/\mathbb{Z}_N$ is given by the A_{N-1} -type ALE space. Since the intersection product of each blow up two-cycle and the four-cycle wrapped by the D4-brane vanishes, wall-crossing phenomena do not occur [60]. This implies that the BPS index of the D4-D2-D0 states is independent of the size of compact two-cycles. In the large radii limit of the two-cycles, the D4-D2-D0 states can be counted in terms of q -deformed Yang-Mills theory [66, 67]. The partition function of the q -deformed Yang-Mills theory is related to the instanton partition function of the Vafa-Witten theory on the A_{N-1} -type ALE space, which is given by the $\widehat{\mathfrak{su}}(N)_1$ -characters [68, 30].

On the other hand, in the small radius limit of the two-cycles, the D4-D2-D0 states are described by our melting crystal model. The absence of wall-crossings implies that the melting crystal model should also reproduce the character of $\widehat{\mathfrak{su}}(N)$. We will explicitly show this below.

From the brane tiling, we find that the supersymmetric quantum mechanics on D2-D0 states is given by the well-known \hat{A}_{N-1} -type quiver [1] with superpotential:

$$W_0 = \sum_{i=0}^{N-1} \text{tr} \Phi_i (X_{i-1} \tilde{X}_{i-1} - \tilde{X}_i X_i). \quad (4.46)$$

The boundary NS5-branes for the lattice point $(1, 0)$ are the first and second ones in the middle picture of figure 38. They generally intersect with each other at N different points in T^2 . The D4-node $*$ is located at one of them. The choice is related to the holonomy of the gauge field at infinity on the D4-brane, which is classified by $\pi_1(S^3/\mathbb{Z}_N) \simeq \mathbb{Z}_N$ [23]. Suppose that our D4-node $*$ is located at the i -th intersection point for some $i = 0, \dots, N-1$. There is a chiral multiplet Φ_i localized at the point. Then the D4-brane induces an additional superpotential

$$W_{\text{flavor}} = \text{tr}(J\Phi_i I). \quad (4.47)$$

We here fix $i = 0$ and consider the corresponding crystal melting model. The other choices of i are realized by shifting the labels of the quiver nodes k as $k \rightarrow k + i \pmod{N}$ in the final expression.

The dimer model and the perfect matching associated with the lattice point $(1, 0)$ are shown in the first and the third picture of the figure 39. The perfect matching contains all the adjoint chiral fields Φ_k , and the constraint (3.6) implies that they have the vanishing vev's:

$$\Phi_k = 0, \quad (k = 0 \dots N-1). \quad (4.48)$$

After eliminating Φ_k from the massless spectrum, the quiver diagram can be depicted as in the left picture of figure 40. The non-trivial F-term conditions are now given by

$$X_{N-1} \tilde{X}_{N-1} - \tilde{X}_0 X_0 + IJ = 0, \quad X_{k-1} \tilde{X}_{k-1} - \tilde{X}_k X_k = 0 \quad (k \neq 0). \quad (4.49)$$

Note here that $J = 0$ also follows on supersymmetric vacua. The two-dimensional crystal for the D4-D2-D0 states is now similar to that in the right picture of figure 28. The only difference is that we here have N different types of box. The melting rule of the crystal now implies that

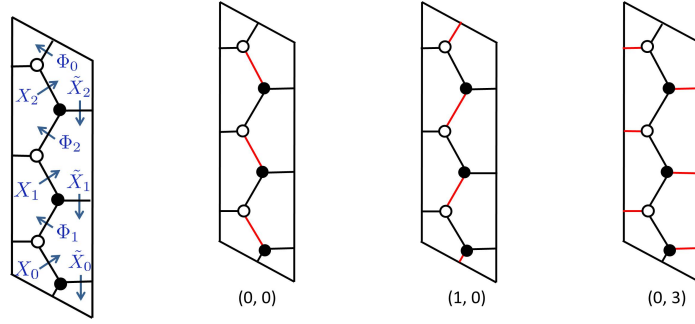


Figure 39: The first: The bipartite graph of $\mathbb{C}^2/\mathbb{Z}_3 \times \mathbb{C}$, which clearly admits an isoradial embedding. The second: The reference perfect matching. The third: The perfect matching associated with the lattice point p_4 . The fourth: The perfect matching associated with the lattice point p_3 .

- Each atom can be removed if and only if its left and lower edges are not attached to other atoms.

Each molten crystal is regarded as a *colored* Young diagram, in which every box has a color. The color of a box atom is determined by the quiver node associated with it. Since we have N quiver nodes besides the D4-node, there are N different colors of box. We call a box “ k -colored box” if it is associated with the k -th quiver node. We show an example of molten crystal in figure 40; white, blue and red boxes represent color 0, 1, 2, respectively.

We here emphasize that the molten configurations of the crystal correspond to the torus fixed point set (orbifold partition) of the ADHM moduli space on the ALE space. Counting the melting crystals is equivalent to evaluating the Euler characteristic of the ADHM moduli space, which is given by the level-one character of $\widehat{\mathfrak{su}}(N)$.

Here, the partition function of the melting crystal is given by

$$\mathcal{Z}_{\text{crystal}} = \sum_{d_0, \dots, d_{N-1}=0}^{\infty} (-1)^{\dim_{\mathbb{C}}(\mathcal{M}_{\vec{d}})} \sum_{\mathcal{P}(\vec{d})} \prod_{k=0}^{N-1} x_k^{d_k}. \quad (4.50)$$

The second summation is taken over the set $\mathcal{P}(\vec{d})$ of all molten configurations with d_k k -colored boxes for $k = 0, \dots, N-1$. We denote by x_k the Boltzmann weight for the k -colored box.

To see that (4.50) is equivalent to the character of $\widehat{\mathfrak{su}}(N)$, we first evaluate the sign factor determined by the dimension of the moduli space. The chiral fields X_k, \tilde{X}_k, I and J contain $\sum_{k=0}^{N-1} 2d_k d_{k-1} + 2d_0$ degrees of freedom. The F-term conditions (4.49)



Figure 40: Left: The reduced quiver diagram of D4-D2-D0 states of $\mathbb{C}^2/\mathbb{Z}_3 \times \mathbb{C}$. Right: A molten configuration for D4-D2-D0 states. Each box has one of the $N = 3$ type color associated with the \mathbb{Z}_3 orbifolding.

reduce $\sum_{i=0}^{N-1} d_i^2$ parameters, and the gauge transformations further reduce the degrees of freedom by d_i^2 . Therefore, the dimension of the moduli space is

$$\dim_{\mathbb{C}}(\mathcal{M}_{\vec{d}}) = \sum_{k=0}^{N-1} (2d_k d_{k-1} - 2d_k^2) + 2d_0. \quad (4.51)$$

This means that the sign factor is

$$(-1)^{\dim_{\mathbb{C}}(\mathcal{M}_{\vec{d}})} = 1. \quad (4.52)$$

We next evaluate the summation over $\mathcal{P}(\vec{d})$ in (4.50). We count the number of colored boxes in a molten configuration. It is shown in [26] that there exists a one-to-one correspondence between the set of the molten configurations $\cup_{\vec{d}} \mathcal{P}(\vec{d})$ and the set

$$\left\{ \vec{k} = (k_0, \dots, k_{N-1}) \in \mathbb{Z}^N \mid \sum_i k_i = 0 \right\} \times \left\{ Y \mid |Y| = nN, n = 0, 1, 2, \dots \right\}, \quad (4.53)$$

with the identification

$$d_i = \frac{1}{2} \sum_{j=0}^{N-1} k_j^2 + \sum_{j=i}^{N-1} k_j + n. \quad (4.54)$$

Here $|Y|$ denotes the total number of boxes in a Young diagram Y . Then the partition function of the melting crystal factorizes into two parts [26]:

$$\mathcal{Z}_{\text{crystal}} = \left(\sum_{\vec{k}: \sum_i k_i = 0} \prod_{i=0}^{N-1} x_i^{\frac{1}{2} \sum_{j=0}^{N-1} k_j^2 + \sum_{j=i}^{N-1} k_j} \right) \left(\sum_{n=0}^{\infty} \sum_{Y: |Y|=nN} (x_0 \cdots x_{N-1})^n \right). \quad (4.55)$$

If we identify the Boltzmann weights of D0-charge and D2-charges as $q = x_0 x_1 \cdots x_{N-1}$ and $Q_i = x_i$, ($i = 1, \dots, N-1$) respectively, the former factor becomes

$$\sum_{\vec{k} \in \mathbb{Z}^N: \sum_i k_i = 0} \prod_{i=0}^{N-1} x_i^{\frac{1}{2} \sum_{j=0}^{N-1} k_j^2 + \sum_{j=i}^{N-1} k_j} = \sum_{(n_1, \dots, n_{N-1}) \in \mathbb{Z}^{N-1}} \prod_{i=1}^{N-1} q^{n_i(n_i - n_{i+1})} Q_i^{n_i}. \quad (4.56)$$

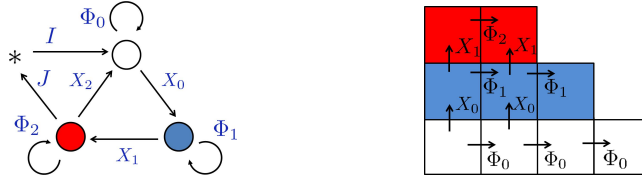


Figure 41: Left: The reduced quiver diagram associated with the lattice point p_3 . Right: A molten configuration.

Here we change the variables as $n_i = \sum_{j=i}^{N-1} k_j$. On the other hand, the latter factor

$$\sum_{n=0}^{\infty} \sum_{Y:|Y|=nN} (x_1 \cdots x_N)^n = \prod_{m=1}^{\infty} \frac{1}{(1 - q^m)^N} \quad (4.57)$$

corresponds to the generating function of the Euler characteristics of the Hilbert schemes of points on the A_{N-1} -type ALE space. Therefore we find that the partition function of the melting crystal is written as

$$\mathcal{Z}_{\text{crystal}} = \frac{q^{\frac{N}{24}}}{\eta(q)^N} \sum_{\mathbf{n} \in \mathbb{Z}^{N-1}} q^{\frac{1}{2} \mathbf{n}^T C \mathbf{n}} \mathbf{Q}^{\mathbf{n}}, \quad (4.58)$$

where C is the A_{N-1} -type Cartan matrix and $\mathbf{Q}^{\mathbf{n}} := \prod_{i=1}^{N-1} Q_i^{n_i}$. This agrees with the level-one character of $\widehat{\mathfrak{su}}(N)$ up to a Q_k -independent prefactor.³⁰

Another melting crystal

We now turn to the second example, in which the D4-brane is wrapping on the non-compact divisor associated with the lattice point $(0, N)$. The topology of the divisor is now $\mathbb{C}/\mathbb{Z}_N \times \mathbb{C}$. In order to be concrete, we will treat the example of $N = 3$. The lattice point corresponding to the divisor is denoted by p_3 in the left picture of figure 38. When we identify the boundary NS5-branes as the first and fifth ones in the second picture of figure 38, \tilde{X}_2 is now identified with X_F . Then the D4-node is now attached to the red and white quiver nodes, and induces the following additional superpotential:

$$W_{\text{flavor}} = J \tilde{X}_2 I. \quad (4.59)$$

³⁰To be precise, we here obtain the level-one character for the trivial weight. The reason for this is that we set $i = 0$ in (4.47). For general i in (4.47), we obtain the character for the i -th level-one weight of $\widehat{\mathfrak{su}}(N)$, up to the n_i -independent overall factor $q^{\frac{i(N-i)}{2N}} e^{\sum_j C_{i,j}^{-1} y_j}$ with $e^{y_j} = Q_j$.

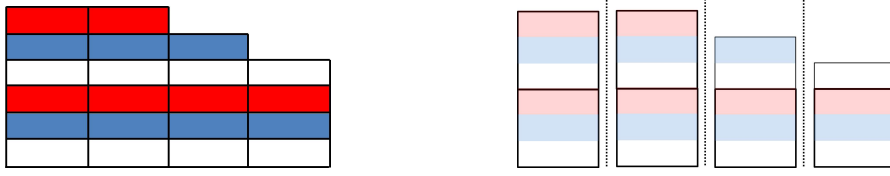


Figure 42: Left: A molten configuration of the crystal. Right: Division of the left picture into towers of atoms. A white, a red and a blue rectangle form a single square.

The perfect matching associated with p_3 is shown in the rightmost picture of the figure 39. Then the constraint (3.6) now requires

$$\tilde{X}_k = 0 \quad (k = 0, 1, 2), \quad (4.60)$$

on supersymmetric vacua. After removing \tilde{X}_k , the quiver diagram can be depicted as in the left picture of 41. The non-trivial F-term conditions become

$$\Phi_1 X_0 - X_0 \Phi_0 = 0, \quad \Phi_2 X_1 - X_1 \Phi_1 = 0, \quad \Phi_0 X_2 - X_2 \Phi_2 + IJ = 0. \quad (4.61)$$

Again, the melting rule of the crystal is the same as for the young diagrams, but the coloring of boxes is different from the previous example; boxes with the same color sit in the horizontal direction (right picture in figure 41).

The partition function of the melting crystal is given by

$$\mathcal{Z}_{\text{crystal}} = \sum_{\mathbf{p}} (-1)^{\dim_{\mathbb{C}}(\mathcal{M}_{d_0, d_1, d_2})} x_0^{d_0} x_1^{d_1} x_2^{d_2}, \quad (4.62)$$

where \mathbf{p} runs over all the molten configurations. The integers d_0 , d_1 and d_2 stand for the numbers of white, blue and red boxes in a molten configuration \mathbf{p} , and x_0 , x_1 and x_2 represent the Boltzmann weights for white, blue and red boxes, respectively. The sign factor is determined as follows. The chiral fields contain the $\sum_{i=0}^2 (d_i d_{i+1} + d_i^2) + d_0 + d_2$ degrees of freedom. The F-term conditions (4.61) reduce $\sum_{i=0}^2 d_i d_{i+1}$ degrees of freedom, and further the gauge transformations reduce $\sum_{i=0}^2 d_i^2$ degrees of freedom. Then the sign becomes

$$(-1)^{\dim_{\mathbb{C}}(\mathcal{M}_{d_0, d_1, d_2})} = (-1)^{d_0 + d_2}. \quad (4.63)$$

We can find the closed expression for the generating function by the similar manner to the second example in subsection 4.3. Let us consider a molten configuration as

in the left picture of figure 42, and divide it into towers of rectangles as in the right picture. We then change the Boltzmann weights as

$$q = x_0 x_1 x_2, \quad Q_1 = -x_0, \quad Q_2 = x_1. \quad (4.64)$$

This means that a square composed of a white, a red and a blue rectangle contributes q to the partition function. An additional white or a blue rectangle contributes Q_1 or Q_2 to the partition function. Thus we have the following three types of tower:

1. A tower which has $k(> 0)$ squares without any additional rectangle on its top. This contributes q^k to the partition function.
2. A tower which has $k(\geq 0)$ squares with an additional white rectangle on its top. This contributes $q^k Q_1$ to the partition function.
3. A tower which has $k(\geq 0)$ squares with an additional white and a blue rectangle on its top. This contributes $q^k Q_1 Q_2$ to the partition function.

The partition function can contain arbitrary number of the three-types of towers, and therefore can be written as

$$\mathcal{Z}_{\text{crystal}} = \prod_{n=1}^{\infty} \frac{1}{1 - q^n} \prod_{m=0}^{\infty} \frac{1}{(1 - q^m Q_1)(1 - q^m Q_1 Q_2)}. \quad (4.65)$$

To see that (4.65) reproduces the correct BPS partition function of the D4-D2-D0 states, we consider the wall-crossing phenomena of BPS states. We consider the blow up geometry of $\mathbb{C}^2/\mathbb{Z}_3 \times \mathbb{C}$ as in figure 43. In the large radii limit of the two-cycles, the divisor wrapped by the D4-brane is isomorphic to \mathbb{C}^2 . Then the D4-D2-D0 state counting reduces the D4-D0 state counting on \mathbb{C}^2 , which again gives the partition function in (4.36). To obtain the partition function in the singular limit, we have to detect the positions of the walls of marginal stability and evaluate the jumps of the BPS indices. The possible decay channels are again written as the following form:

$$\Gamma \rightarrow \Gamma_1 + \Gamma_2 \quad (4.66)$$

with

$$\Gamma = \mathcal{D} + \sum_{k=1}^2 M_k \beta_k - NdV, \quad \Gamma_2 = \sum_{k=1}^2 m_k \beta_k + ndV. \quad (4.67)$$

The Gopakumar-Vafa invariants tell us that the non-vanishing BPS indices are now

$$\Omega(\Gamma_2) = 1 \quad \text{for} \quad (m_1, m_2, n) = (\pm 1, 0, n), (0, \pm 1, n), (\pm 1, \pm 1, n). \quad (4.68)$$

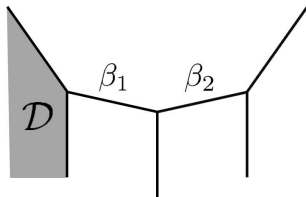


Figure 43: The web diagram of blow up geometry of $\mathbb{C}^2/\mathbb{Z}_3 \times \mathbb{C}$. The grey region \mathcal{D} represents the toric divisor wrapped by the D4-brane. In the singular limit, the topology of \mathcal{D} becomes $\mathbb{C}/\mathbb{Z}_3 \times \mathbb{C}$. The β_1 and β_2 represent the blow up compact two-cycles.

We have the walls of marginal stability for $(m_1, m_2, n) = (\pm 1, 0, n), (0, \pm 1, n), (\pm 1, \pm 1, n)$. The position of the walls are identified by solving (4.37). When we fix $z_2 = \frac{1}{2}$, the locations of the walls are the same as in figure 37. However, the intersection products between β_k and \mathcal{D} are different from those in subsection 4.3:

$$\langle \mathcal{D}, \beta_1 \rangle = 1, \quad \langle \mathcal{D}, \beta_2 \rangle = 0, \quad (4.69)$$

Using the wall-crossing formula (4.43), we find that the BPS partition function at the orbifold limit is written as

$$\begin{aligned} \mathcal{Z}_{\text{D4-D2-D0}} &= \mathcal{Z}_0 \prod_{m=0}^{\infty} \frac{1}{(1 - q^m Q_1)(1 - q^m Q_1 Q_2)} \\ &= \prod_{n=1}^{\infty} \frac{1}{1 - q^n} \prod_{m=0}^{\infty} \frac{1}{(1 - q^m Q_1)(1 - q^m Q_1 Q_2)}, \end{aligned} \quad (4.70)$$

which coincides with (4.65).

We here comment on the relation to the instanton counting on $\mathbb{C}/\mathbb{Z}_N \times \mathbb{C}$. As the orbifold partitions are in one-to-one correspondence with the torus fixed points of the moduli space of instantons on $\mathbb{C}^2/\mathbb{Z}_N$, the molten crystals we are considering here correspond to the fixed points of the moduli space of instantons on $\mathbb{C}/\mathbb{Z}_N \times \mathbb{C}$ [69].

Acknowledgments

We would like to thank Richard Eager, Tohru Eguchi, Daigo Honda, Yosuke Imamura, Tetsuji Kimura, Kazutoshi Ohta, Kazushi Ueda and Masahito Yamazaki for illuminating discussions and important comments. The work of T.N. is supported in part by the U.S. Department of Energy under grant DE-FG02-96ER40959. The work of

T.N. was supported in part by Center for Quantum Spacetime during his stay there before September 2012. S.Y. was supported in part by KAKENHI 22740165.

A Stability condition

In [4], the slope function is defined by

$$\mu_{\vartheta}(M) := \frac{\sum_{\ell \in \widehat{Q}_0} \vartheta_{\ell} \dim M_{\ell}}{\sum_{\ell \in \widehat{Q}_0} \dim M_{\ell}}, \quad (\text{A.1})$$

and M is called ϑ -stable if every non-zero proper submodule $N \subset M$ satisfy $\mu_{\vartheta}(N) < \mu_{\vartheta}(M)$. The ϑ -parameters are set in [4] so that $\vartheta_* = 1$ and $\vartheta_k = 0$ for $k \in Q_0$. We here describe that the θ -stability we use in this paper is equivalent to this ϑ -stability.

First of all, the ϑ -stability is invariant under the following two types of change

- $\vartheta \rightarrow \vartheta + \zeta$ for any $\zeta \in \mathbb{R}$,
- $\vartheta \rightarrow \xi \vartheta$ for any $\xi \in \mathbb{R}_+$.

We particularly use the first one. For a given A -module M , let us define $\vartheta' := \vartheta + \zeta$ with

$$\zeta = -\frac{\sum_{\ell \in \widehat{Q}_0} \vartheta_{\ell} \dim M_{\ell}}{\sum_{\ell \in \widehat{Q}_0} \dim M_{\ell}}. \quad (\text{A.2})$$

Then the ϑ' -stability of M is equivalent to the ϑ -stability of M . Note that we have $\mu_{\vartheta'}(M) = 0$, and therefore $\mu_{\vartheta}(N) < \mu_{\vartheta}(M)$ is equivalent to $\mu_{\vartheta'}(N) < 0$.

We now identify our θ as $\theta = \vartheta'$. Although our slope function $\theta(M)$ is different from $\mu_{\vartheta}(M)$, we can easily show that $\theta(N) < 0$ is equivalent to $\mu_{\vartheta}(N) < 0$. Hence, our θ -stability is equivalent to the original ϑ -stability. Furthermore, it follows from $\theta = \vartheta + \zeta$ that $\vartheta_* = 1, \vartheta_k = 0$ implies $\theta_* \geq 0, \theta_k < 0$.

B Isoradial dimer model

The necessary and sufficient condition for a dimer model Q^{\vee} on T^2 to admit an isoradial embedding was given in Theorem 5.1 of [70]. The condition is rephrased in terms of zig-zag paths as follows:³¹

³¹For the definition of zig-zag paths, see subsection 3.5.

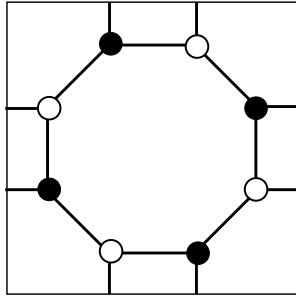


Figure 44: An example of dimer model which does not admit any isoradial embedding, which is associated with the local $\mathbb{P}^1 \times \mathbb{P}^1$.

- Any zig-zag path of Q^\vee is a closed curve without self-intersection,
- In the universal cover \tilde{Q}^\vee , any two zig-zag paths share at most one edge.

All the dimer models shown in this paper admit an isoradial embedding. On the other hand, for example, the dimer model in figure 44 does not admit any isoradial embedding. In fact, there are pairs of zig-zag paths in the universal cover which share an infinite number of edges.

C Perfect matching and toric divisor

When we consider a single D0-brane probe on the Calabi-Yau singularity Y_Σ , the condition (3.6) is understood as the condition that the D0-probe is moving in the divisor \mathcal{D} . We here describe this.

Let us first note that the chiral multiplets $X_a \in Q_1$ are expressed by commutative complex variables if we only have a single D0-probe. In this case, the F-term conditions *without* flavor branes are known to be solved by [71, 18, 52]

$$X_a = \prod_{m \ni X_a} p_m, \tag{C.1}$$

where the product runs over the perfect matchings involving X_a . The variable p_m is a complex variable and regarded as a new “field” associated with the perfect matching m . These new fields in fact trivialize all the F-term conditions $\partial W_0 / \partial X_a = 0$. Therefore, we can regard p_m as the fields of a gauged linear sigma model without superpotential. The moduli space of the sigma model corresponds to the background Calabi-Yau geometry Y_Σ in which the D0-probe is moving.

Now, let us consider the condition (3.6). In the D0-probe setup, the condition is equivalent to

$$p_{m_{\mathcal{D}}} = 0. \tag{C.2}$$

It was shown in [72] that,³² when \mathcal{D} is associated with a corner of the toric diagram, this condition describes the divisor \mathcal{D} in the moduli space of the gauged linear sigma model. This is physically interpreted to mean that the D0-probe should move in the divisor \mathcal{D} in order to keep the BPS condition with a D4-brane wrapping on \mathcal{D} .

References

- [1] M. R. Douglas and G. W. Moore, “D-branes, quivers, and ALE instantons,” hep-th/9603167.
- [2] A. Okounkov, N. Reshetikhin and C. Vafa, “Quantum Calabi-Yau and classical crystals,” *Progr. Math.* **244** (2006) 597 [hep-th/0309208].
- [3] B. Szendrői, “Non-commutative Donaldson-Thomas theory and the conifold,” *Geom. Topol.* **12**, 1171 (2008) [arXiv:0705.3419 [math.AG]].
- [4] S. Mozgovoy and M. Reineke, “On the noncommutative Donaldson-Thomas invariants arising from brane tilings,” arXiv:0809.0117 [math.AG].
- [5] H. Ooguri and M. Yamazaki, “Crystal Melting and Toric Calabi-Yau Manifolds,” *Commun. Math. Phys.* **292** (2009) 179 [arXiv:0811.2801 [hep-th]].
- [6] M. Aganagic and K. Schaeffer, “Wall Crossing, Quivers and Crystals,” *JHEP* **1210** (2012) 153 [arXiv:1006.2113 [hep-th]].
- [7] W. -y. Chuang and D. L. Jafferis, “Wall Crossing of BPS States on the Conifold from Seiberg Duality and Pyramid Partitions,” *Commun. Math. Phys.* **292** (2009) 285 [arXiv:0810.5072 [hep-th]].
- [8] W. -y. Chuang and G. Pan, “BPS State Counting in Local Obstructed Curves from Quiver Theory and Seiberg Duality,” *J. Math. Phys.* **51** (2010) 052305 [arXiv:0908.0360 [hep-th]].

³²In particular, see appendix A.2.

- [9] P. Sulkowski, “Wall-crossing, free fermions and crystal melting,” *Commun. Math. Phys.* **301** (2011) 517 [arXiv:0910.5485 [hep-th]].
- [10] T. Dimofte and S. Gukov, “Refined, Motivic, and Quantum,” *Lett. Math. Phys.* **91** (2010) 1 [arXiv:0904.1420 [hep-th]].
- [11] A. Iqbal, N. Nekrasov, A. Okounkov and C. Vafa, “Quantum foam and topological strings,” *JHEP* **0804** (2008) 011 [hep-th/0312022].
- [12] H. Ooguri and M. Yamazaki, “Emergent Calabi-Yau Geometry,” *Phys. Rev. Lett.* **102** (2009) 161601 [arXiv:0902.3996 [hep-th]].
- [13] T. Nishinaka and S. Yamaguchi, “Statistical model and BPS D4-D2-D0 counting,” *JHEP* **1105** (2011) 072 [arXiv:1102.2992 [hep-th]].
- [14] T. Nishinaka and Y. Yoshida, “A Note on statistical model for BPS D4-D2-D0 states,” *Phys. Lett. B* **711** (2012) 132 [arXiv:1108.4326 [hep-th]].
- [15] H. Nakajima, “Lectures on Hilbert Schemes of Points on Surfaces,” , American Mathematical Society, University Lectures Series (1999).
- [16] N. A. Nekrasov, “Seiberg-Witten prepotential from instanton counting,” *Adv. Theor. Math. Phys.* **7** (2004) 831 [hep-th/0206161].
- [17] A. Hanany and K. D. Kennaway, “Dimer models and toric diagrams,” hep-th/0503149.
- [18] S. Franco, A. Hanany, K. D. Kennaway, D. Vegh and B. Wecht, “Brane dimers and quiver gauge theories,” *JHEP* **0601** (2006) 096 [hep-th/0504110].
- [19] S. Franco, A. Hanany, D. Martelli, J. Sparks, D. Vegh and B. Wecht, “Gauge theories from toric geometry and brane tilings,” *JHEP* **0601** (2006) 128 [hep-th/0505211].
- [20] A. Hanany and D. Vegh, “Quivers, tilings, branes and rhombi,” *JHEP* **0710** (2007) 029 [hep-th/0511063].
- [21] K. D. Kennaway, “Brane Tilings,” *Int. J. Mod. Phys. A* **22** (2007) 2977 [arXiv:0706.1660 [hep-th]].

- [22] M. Yamazaki, “Brane Tilings and Their Applications,” *Fortsch. Phys.* **56** (2008) 555 [arXiv:0803.4474 [hep-th]].
- [23] S. Franco and A. M. Uranga, “Dynamical SUSY breaking at meta-stable minima from D-branes at obstructed geometries,” *JHEP* **0606** (2006) 031 [hep-th/0604136].
- [24] N. Broomhead, “Dimer models and Calabi-Yau algebras,” arXiv:0901.4662.
- [25] F. Fucito, J. F. Morales and R. Poghossian, “Multi instanton calculus on ALE spaces,” *Nucl. Phys. B* **703** (2004) 518 [hep-th/0406243].
- [26] S. Fujii and S. Minabe, “A Combinatorial Study on Quiver Varieties,” [math/0510455].
- [27] R. Dijkgraaf and P. Sulkowski, “Instantons on ALE spaces and orbifold partitions,” *JHEP* **0803** (2008) 013 [arXiv:0712.1427 [hep-th]].
- [28] N. Nekrasov and A. Okounkov, “Seiberg-Witten theory and random partitions,” hep-th/0306238.
- [29] L. F. Alday, D. Gaiotto and Y. Tachikawa, “Liouville Correlation Functions from Four-dimensional Gauge Theories,” *Lett. Math. Phys.* **91** (2010) 167 [arXiv:0906.3219 [hep-th]].
- [30] C. Vafa and E. Witten, “A Strong coupling test of S duality,” *Nucl. Phys. B* **431**, 3 (1994) [hep-th/9408074].
- [31] M. Cirafici, A. -K. Kashani-Poor and R. J. Szabo, “Crystal melting on toric surfaces,” *J. Geom. Phys.* **61** (2011) 2199 [arXiv:0912.0737 [hep-th]].
- [32] R. J. Szabo, “Crystals, instantons and quantum toric geometry,” *Acta Phys. Polon. Supp.* **4** (2011) 461 [arXiv:1102.3861 [hep-th]].
- [33] M. Cirafici and R. J. Szabo, “Curve counting, instantons and McKay correspondences,” arXiv:1209.1486 [hep-th].
- [34] W. -y. Chuang, D. -E. Diaconescu, J. Manschot, G. W. Moore and Y. Soibelman, “Geometric engineering of (framed) BPS states,” arXiv:1301.3065 [hep-th].

- [35] T. Maeda, T. Nakatsu, K. Takasaki and T. Tamakoshi, “Five-dimensional supersymmetric Yang-Mills theories and random plane partitions,” *JHEP* **0503** (2005) 056 [hep-th/0412327].
- [36] T. Maeda, T. Nakatsu, K. Takasaki and T. Tamakoshi, “Free fermion and Seiberg-Witten differential in random plane partitions,” *Nucl. Phys. B* **715** (2005) 275 [hep-th/0412329].
- [37] T. Maeda, T. Nakatsu, Y. Noma and T. Tamakoshi, “Gravitational quantum foam and supersymmetric gauge theories,” *Nucl. Phys. B* **735** (2006) 96 [hep-th/0505083].
- [38] T. Maeda and T. Nakatsu, “Amoebas and instantons,” *Int. J. Mod. Phys. A* **22** (2007) 937 [hep-th/0601233].
- [39] T. Nakatsu and K. Takasaki, “Melting crystal, quantum torus and Toda hierarchy,” *Commun. Math. Phys.* **285** (2009) 445 [arXiv:0710.5339 [hep-th]].
- [40] S. Benvenuti, B. Feng, A. Hanany and Y. -H. He, “Counting BPS Operators in Gauge Theories: Quivers, Syzygies and Plethystics,” *JHEP* **0711** (2007) 050 [hep-th/0608050].
- [41] Y. Noma, T. Nakatsu and T. Tamakoshi, “Plethystics and instantons on ALE spaces,” hep-th/0611324.
- [42] D. Forcella, A. Hanany and A. Zaffaroni, “Baryonic Generating Functions,” *JHEP* **0712** (2007) 022 [hep-th/0701236 [HEP-TH]].
- [43] A. Butti, D. Forcella, A. Hanany, D. Vegh and A. Zaffaroni, “Counting Chiral Operators in Quiver Gauge Theories,” *JHEP* **0711** (2007) 092 [arXiv:0705.2771 [hep-th]].
- [44] H. Ooguri and C. Vafa, “Two-dimensional black hole and singularities of CY manifolds,” *Nucl. Phys. B* **463** (1996) 55 [hep-th/9511164].
- [45] A. Hanany and A. M. Uranga, “Brane boxes and branes on singularities,” *JHEP* **9805** (1998) 013 [hep-th/9805139].
- [46] B. Feng, Y. -H. He, K. D. Kennaway and C. Vafa, “Dimer models from mirror symmetry and quivering amoebae,” *Adv. Theor. Math. Phys.* **12** (2008) 489 [hep-th/0511287].

- [47] Y. Imamura, “Anomaly cancellations in brane tilings,” JHEP **0606** (2006) 011 [hep-th/0605097].
- [48] A. D. King, “Moduli of representations of finite dimensional algebras,” Quart. J. Math. Oxford **45**, 515 (1994).
- [49] K. Larjo, “Consistently melting crystals,” arXiv:0902.0614 [hep-th].
- [50] A. Ishii and K. Ueda, “A note on consistency conditions on dimer models,” RIMS Kokyuroku Bessatsu **B24** (2011) 143-164 [arXiv:1012.5449 [math.AG]]
- [51] D. R. Gulotta, “Properly ordered dimers, R-charges, and an efficient inverse algorithm,” JHEP **0810** (2008) 014 [arXiv:0807.3012 [hep-th]].
- [52] S. Franco and D. Vegh, “Moduli spaces of gauge theories from dimer models: Proof of the correspondence,” JHEP **0611** (2006) 054 [hep-th/0601063].
- [53] A. Hanany and D. Tong, “Vortices, instantons and branes,” JHEP **0307** (2003) 037 [hep-th/0306150].
- [54] S. Shadchin, “On F-term contribution to effective action,” JHEP **0708**, 052 (2007) [hep-th/0611278].
- [55] T. Dimofte, S. Gukov and L. Hollands, “Vortex Counting and Lagrangian 3-manifolds,” Lett. Math. Phys. **98**, 225 (2011) [arXiv:1006.0977 [hep-th]].
- [56] Y. Yoshida, “Localization of Vortex Partition Functions in $\mathcal{N} = (2, 2)$ Super Yang-Mills theory,” arXiv:1101.0872 [hep-th].
- [57] A. Hanany, C. P. Herzog and D. Vegh, “Brane tilings and exceptional collections,” JHEP **0607** (2006) 001 [hep-th/0602041].
- [58] T. Nishinaka and S. Yamaguchi, “Wall-crossing of D4-D2-D0 and flop of the conifold,” JHEP **1009** (2010) 026 [arXiv:1007.2731 [hep-th]].
- [59] T. Nishinaka, “Multiple D4-D2-D0 on the Conifold and Wall-crossing with the Flop,” JHEP **1106** (2011) 065 [arXiv:1010.6002 [hep-th]].
- [60] T. Nishinaka and S. Yamaguchi, “Affine $SU(N)$ algebra from wall-crossings,” arXiv:1107.4762 [hep-th].

- [61] T. Nishinaka, T. Okada, T. Okazaki and S. Yamaguchi, “Evidence for Duality of Conifold from Fundamental String,” JHEP **1110** (2011) 051 [arXiv:1107.3660 [hep-th]].
- [62] D. L. Jafferis and G. W. Moore, “Wall crossing in local Calabi Yau manifolds,” arXiv:0810.4909 [hep-th].
- [63] R. Gopakumar and C. Vafa, “M theory and topological strings. 1.,” hep-th/9809187.
- [64] R. Gopakumar and C. Vafa, “M theory and topological strings. 2.,” hep-th/9812127.
- [65] F. Denef and G. W. Moore, “Split states, entropy enigmas, holes and halos,” JHEP **1111** (2011) 129 [hep-th/0702146 [HEP-TH]].
- [66] M. Aganagic, H. Ooguri, N. Saulina and C. Vafa, “Black holes, q-deformed 2d Yang-Mills, and non-perturbative topological strings,” Nucl. Phys. B **715**, 304 (2005) [hep-th/0411280].
- [67] M. Aganagic, D. Jafferis and N. Saulina, “Branes, black holes and topological strings on toric Calabi-Yau manifolds,” JHEP **0612**, 018 (2006) [hep-th/0512245].
- [68] H. Nakajima, Instantons on ALE spaces, quiver varieties and Kac-Moody algebras, Duke Math. J. **76** (1994) 365.
- [69] H. Kanno and Y. Tachikawa, “Instanton counting with a surface operator and the chain-saw quiver,” JHEP **1106**, 119 (2011) [arXiv:1105.0357 [hep-th]].
- [70] R. Kenyon and J. -M. Schlenker, “Rhombic embeddings of planar quad-graphs,” Trans. Amer. Math. Soc. **357** (2005) 3443 [math-ph/0305057].
- [71] B. Feng, A. Hanany and Y. -H. He, “Phase structure of D-brane gauge theories and toric duality,” JHEP **0108** (2001) 040 [hep-th/0104259].
- [72] Y. Imamura, K. Kimura and M. Yamazaki, “Anomalies and O-plane charges in orientifolded brane tilings,” JHEP **0803** (2008) 058 [arXiv:0801.3528 [hep-th]].